Journal of Applied Fluid Mechanics, Vol. 17, No. 8, pp. 1568-1592, 2024.
Available online at www.jafmonline.net, ISSN 1735-3572, EISSN 1735-3645.
https://doi.org/10.47176/jafm.17.8.2490

Numerical Analysis of the Kline and Fogleman Airfoil's Effect on the Operation of Straight Darrieus Wind Turbine

H. Iddou[1†], N. Nait Bouda[1], A. Benaissa[2] and K. Zereg[3]

[1] *University of Science and Technology Houari Boumediene (USTHB), Bab Ezzouar, Algiers, 16111, Algeria*
[2] *Royal Military College of Canada, Station Forces Kingston, Ontario, K7K 7B4, Canada*
[3] *University of Batna1, Batna, Batna, 05000, Algeria*

†*Corresponding Author Email: hiddou@usthb.dz*

ABSTRACT

The blade profile selection is paramount for the efficient operation of straight Darrieus wind turbines in terms of torque and power generation. In this work, we have used the Kline-Fogleman Airfoil (KFA) design for the wind turbine blades. The concept of KFA design aims to cause flow separation, vortex formation, and reattachment establishment before the trailing edge. Thus, geometric tests on have been performed on the baseline airfoil NACA0015 as one of the best profiles for operating a straight Darrius wind turbine. A two-dimensional Computational Fluid Dynamic (CFD) model using the two-equation Shear Stress Transport k-ω (SST k-ω) turbulent model was developed in ANSYS/FLUENT software to assess the aerodynamic efficiency of the modified airfoil. Two designs (KFA-2 and KFA-4) were tested initially in the static case. The effects of the opening step angle and its curvature diameter were studied for an angle of attack's range of -20° to +20°. The rounded KFA-4 design with an opening step angle of 93.6° led to a significant improvement in the lift-to-drag ratio thus, aerodynamic efficiency. Finally, the straight KFA-4 design with the opening step angle of 93.6° revealed a the most advantageous effects on the operation of a straight Darrieus wind turbine for a Tip Speed Ratio less than 1.6 (TSR<1.6). It allowed a noticeable reduction of the dead zone and TSR corresponding to the nominal power, thus consequently improving the starting torque and delaying torque stall.

Article History

Received December 9, 2023
Revised February 27, 2024
Accepted March 11, 2024
Available online May 29, 2024

Keywords:

Straight Darrieus wind turbine
Turbulence modeling
Computational fluid dynamics
Passive flow control
Aerodynamic coefficients
Dynamic stall

1. INTRODUCTION

The increase in renewable energy usage, such as wind and solar power worldwide, is substantial in the present context not only due to the negligible amount of greenhouse gases emitted during their use but also because of their sustainable nature, unlike fossil fuels. For these reasons, industries, companies, and individuals are interested in the use of mechanical, electrical, or hybrid (mechanical/electrical) devices that could harness the energy coming from renewable resources (Qadri et al., 2019; Akhlaghi et al., 2023; Cardoso Netto et al., 2023). Wind energy is an attractive option due to its vast availability, commercially ready technology, low cost, and significant contribution to CO_2 reduction. As a mechanical device designed to convert a part of the wind's kinetic energy into valuable electrical energy, the wind turbine is the most important component of the wind energy system.

The straight Darrieus Vertical Axis Wind Turbine (SD-VAWT) is widely used in the industrial and private sectors due to the operational independence from the wind direction and its low cost in terms of design, installation, and maintenance (Mohammed et al., 2019; Mohan Kumar et al., 2019). This kind of wind turbine, known as a lift type, uses aerodynamic lift force to generate power. Therefore, the blade profile directly influences the performance of SD-VAWT (Moghimi & Motawej, 2020).

The choice of the blade shape is the most important step in the VAWT design. Therefore, several studies have been focused on the effect of the blade profile on the power curve of the SD-VAWT. Mohamed (2012) carried out a numerical investigation using CFD to compare the nominal powers of 20 different symmetrical and asymmetrical profiles from various families, including NACA, Fx, S, and AH. His results show that symmetrical airfoils are more efficient than asymmetrical ones, and the S-1046 is the most efficient profile, with a relative

NOMENCLATURE

α	angle of attack	V_∞	free stream velocity
α^+	positive angle of attack	**ABBREVIATION**	
α^-	negative angle of attack	AOA	Angle Of Attack
ω_z	z-vorticity	ASA	Acute Step Angle
Ψ	opening step angle	BEM	Blade Element Momuntum
θ	azimuth angle	CFD	Computational Fluid Dynamics
C_D	drag coefficient	KFA	Kline Fogleman Airfoil
C_L	lift force	OSA	Obtuse Step Angle
C_L/C_D	aerodynamic efficiency	SD-VAWT	Straight Darrieus Vertical Axis Wind Turbine
C_m	torque coefficient	LVAWT	Lift Vertical Axis Wind Turbine
C_P	power coefficient	RSA	Right Step Angle
TSR	Tip Speed Ratio	URANS	Unsteady Reynolds-Averaged Navier-Stokes

increase of 26.83% compared to symmetrical NACA profiles. In the numerical study of Danao et al. (2012), using the Shear Stress Transport (SST) k-ω turbulent model, they compared the performance of symmetrical and cambered airfoils. Their results showed that the symmetrical airfoil blade design is the most advantageous. Roh and Kang (2013) have used the semi-empirical method of Multiple Stream Tube (MST) to study the effect of the maximum relative thickness of symmetrical profiles NACA00XX on the performance of straight VAWTs. They concluded that the thick profiles are better at low tip speed ratio (TSR) and that the thin ones are advantageous at high TSR and have difficulty in self-starting. Overall, the NACA0015 profile has an excellent operational performance over the whole range of the studied TSR. Subramanian et al. (2017), Wang et al. (2018), and Song et al. (2020) have well confirmed these results using CFD in ANSYS/FLUENT software, and they have mentioned that the thick profiles are better for VAWT self-starting.

The complexity of the flow around the SD-VAWT results from the cyclic variation of the relative velocity direction on the blade and its magnitude during the rotation. The relative angle of attack exceeds the positive and negative static stall at a low tip speed ratio (TSR), which causes difficulty in starting torque generation and the separation of the flow from the blade surface; the latter leads to dynamic stall and generates blade/wake interference which is the main reason for the low energy extraction and failure of the VAWT elements (Sagharichi et al., 2016; Zhao et al., 2018, 2022). To improve the aerodynamic performance of wind turbines, many studies have been devoted to controlling the development of the boundary layer on the blade. In our case, we are interested in passive control that avoids using an external energy source to improve the SD-VAWT's self-starting and/or nominal power. Many researchers have focused on making its operation more profitable at low tip speed ratios and minimizing its dead zone (Zhang et al., 2020; Manerikar et al., 2021; Syawitri et al., 2022; Truong et al., 2022). The aerodynamic coefficients measurements made by Storms and Jang (1994) on the static NACA4412 airfoil with and without the Gurney flap on the lower surface near the trailing edge showed that the Gurney flap improves the aerodynamic performance by 31.54% compared to the baseline profile. Later, Jang et al. (1998) numerically studied the effect of the Gurney flap installed at the trailing edge of the underside surface of the static NACA4412 airfoil. Their results showed that the Gurney flap improved the aerodynamic performance of the baseline NACA4412 airfoil, as in Storms and Jang (1994). Xie et al. (2016) investigated the effect of the Gurney flap height on the improvement of energy extraction of the oscillating airfoil NACA0012. The authors concluded that the Gurney flap benefits lift generation and that the most optimal flap height is 3% of the chord. The effect of a semicircular cavity on the upper surface of a static NACA0018 profile was numerically investigated by Olsman and Colonius (2011). The authors concluded that the vortices generated by the cavity delay the flow's separation and accelerate the motion of the small vortex structures near the wall. This leads to a delay in the dynamic stall and drag reduction, thus improving aerodynamic performance. A CFD study on the effect of a cavity's geometric shape, diameter, and location on the performance of a SD-VAWT with NACA0021 blade profile was conducted by Sobhani et al. (2017). They found that the most optimal configuration has a 25% power improvement over the basic design. It corresponds to a semicircular cavity with a diameter of 8% of the chord, with its center at the maximum camber position of the airfoil. (Ismail & Vijayaraghavan, 2015) investigated the combination of the inward semicircular dimple and the Gurney flap on the underside surface of the VAWT blades with the NACA0015 profile. The modifications performed resulted in a 40% increase in the generated torque at $Re_c=2.55\times10^5$ and TSR=3.5. To improve the starting torque and the nominal power of a SD-VAWT, Zamani et al., (2016a) have modified the Du 06-W-200 J-shaped profile. This technique eliminates the pressure side of the profile from the maximum thickness to the trailing edge. The results show that the modification improves the self-starting and the nominal power by 3% compared to the conventional profile Du 06-W-200. This technique was applied to another prototype profiled by NACA0015, which improved the power curve and 6% of the nominal power (Zamani et al., 2016b). By modifying the mean camber line of a NACA0018 SD-VAWT blade profile, Ma *et al.* (2018) improved the power of SD-VAWT by 26.82% compared to the baseline prototype.

The report of the United States patent performed by Fertis (1986) covers the effect of the inclination of the straight step, located at 50% of the chord with a depth of

25% of the local step thickness. The results show that the step eliminates dynamic stall for the static airfoil NACA23012 and that the inclined step performs better than the horizontal step over a wide range of angles of attack α and Reynolds numbers Re_c. Arun Prakash et al. (2017) conducted an experimental study on the effect of mid-chord step on the performance of three-bladed horizontal axis wind turbines with NACA0012 and NACA23012 airfoils. Their results show that the airfoils with mid-chord step perform better than the conventional airfoils over the range of rotational speeds tested (between 600 and 1500 RPM). The effect of the step depth on the lift generation has been considered by Sammak et al. (2012) and Boroomand and Hosseinverdi (2009). their results show that increasing the depth step on the upper surface has positively impacts the lift improvement for negative angles of attack and a negative impact on positive ones. It is also found that the lift-to-drag ratio decreases with the relative local thickness. A combination between half of the NACA0012 profile and half of the NACA0006 profile results in a NACA0012 airfoil with two steps at mid-chord, one on the upper surface and the other on the lower surface. This modification improved the energy extraction of the oscillating airfoil by 30.60% and 17.32% over NACA0006 and NACA0012, respectively (Boudis et al., 2018). Frunzulica et al. (2014) conducted a comparative study between three modifications applied to a vertical axis wind turbine blade profiled by NACA0012. These consist of a 50% chord step on the upper surface, a semicircular turbulence promoter at the leading edge, and a slot on the upper surface of the blade. The CFD results indicate that all three modifications positively improve the wind turbine starting torque and that the profile with a step is the most optimal choice. Aziz and Islam (2017) have experimentally compared the aerodynamic coefficients of the NACA4415 airfoil with and without a step on the underside surface. The step with a depth of 5.5% chord resulted, for a range of angles of attack $0° \leq \alpha \leq 18°$, in a 2.69% increase in aerodynamic efficiency compared to the baseline airfoil.

A literature review of Passive Flow Control Devices (PFCDs) implemented on lift VAWTs (LVAWTs) was provided by Zhao et al. (2022). However, their review was quite limited, and they briefly explained the application of PFCDs and how they can improve the performance of LVAWTs. A more extended review was later provided by Syawitri et al. (2022). From the literature of the matter at hand, it is noticed that the Kline and Fogleman Airfoil (KFA) design application to SD-VAWT has not received as much attention as other PFCDs, despite KFA's proven enhancement of the lift-to-drag coefficient and the overall aerodynamic performance of LVAWTs, making it a promising solution in the context solution in the context of wind energy extraction trough airfoil geometrical modification (Frunzulica et al., 2014; Syawitri et al., 2022; Zhao et al., 2022). That is the aim of the present study.

Our research presents a parametric study of the blade of a straight Darrieus wind turbine using two types of Kline and Flogleman Airfoil modifications and assesses its effect on the aerodynamic coefficients of the static blade profile (for various angles of attack), as well as on the torque generation, and power curve for dynamic straight Darrieus VAWT (at different TSRs values). Special emphasis is also given to the analysis of the opening step angle effect, the type of modification (KFA-2 and KFA-4), and the effect of the step geometric shape on the static and dynamic blade performance.

2. METHODOLOGY

2.1 Technique and Calculation Methods

The numerical prediction of the power curve of a SD-VAWT requires using Blade Element Momentum (BEM) or Computational Fluid Dynamic (CFD). The BEM is a semi-empirical method based on algorithms that use experimental data for the prediction of aerodynamic forces and power curve, such as the Multiple Stream Tube (MST) and Double Multiple Stream Tube (DMST) methods (Roh and Kang, 2013; Meana-Fernández et al., 2018). The CFD approach uses the finite volume method to solve the conservative Navier-Stokes equations in a fluid domain around the SD-VAWT to obtain the pressure/velocity distribution and predict the evolution of the aerodynamic and power coefficient (Modi & Gilke, 2018). Compared to BEM methods, CFD has a good ability to predict the power coefficient, the blade-vortex interaction, and the wake (Kozak et al., 2016). Several techniques have been used for this purpose, such as the six degrees of freedom (6DOF), sliding mesh, and overset mesh (Wang et al., 2011; Wekesa et al., 2015; Lopez Mejia et al., 2021). In the present study, we chose the sliding mesh method because the 6DOF method is costly in terms of computational resources, and the overset mesh method is limited in terms of choice of turbulence model, velocity-pressure decoupling methods, and space-time discretization schemes on the ANSYS/FLUENT software.

2.2 Governing Equations

The 2D numerical simulations of the unsteady and incompressible airflow around a straight VAWT prototype were performed by discretization of the conservative averaged Navier Stokes equations (Eq.1 and Eq.2) using finite volume method via ANSYS/FLUENT 14.0 software.

$$\frac{\partial \overline{u_i}}{\partial x_i} = 0 \tag{1}$$

$$\frac{\partial \overline{u_i}}{\partial t} + \overline{u_j}\frac{\partial \overline{u_i}}{\partial x_j} = -\frac{1}{\rho}\frac{\partial \overline{P}}{\partial x_i} + \frac{\partial}{\partial x_j}\left[\nu \frac{\partial \overline{u_i}}{\partial x_j} - \overline{u_i' u_j'}\right] \tag{2}$$

2.2.1 Turbulence Modeling

The closure of the Unsteady Reynolds Averaged Navier Stokes (URANS) equations system is ensured by the Shear Stress Transport (SST) k-ω model developed by Menter in 1994. This model is based on the turbulent viscosity concept, which requires the solution of two transport equations for the turbulent kinetic energy k and the turbulent energy dissipation rate ω (Eq.3 and Eq.4). This model uses a blend function of the two models k-ϵ to predict the free shear layers away from the wall with a relatively small pressure gradient, and k-ω to predict the sub-boundary layer near-wall (Menter, 1994; Apsley &

Table 1 Additional SST k-ω model constants

α_1	α_2	β_1	β_2	β^*	σ_{k1}	σ_{k2}	$\sigma_{\omega1}$	$\sigma_{\omega2}$
1	0.52	0.075	0.0828	0.09	1.176	1	2	1.168

Leschziner, 2000; ANSYS Fluent UG, 2011; Rumsey, 2017).

$$\frac{\partial k}{\partial t}+\frac{\partial\left(\overline{u_j}k\right)}{\partial x_j}=\frac{P}{\rho}-\beta\omega k+\frac{\partial\left[\left(\nu+\sigma_k\nu_t\right)\frac{\partial k}{\partial x_j}\right]}{\partial x_j} \tag{3}$$

$$\frac{\partial \omega}{\partial t}+\frac{\partial\left(\overline{u_j}\omega\right)}{\partial x_j}=\frac{\gamma}{\nu_t}P-\beta\omega^2+\frac{\partial\left[\left(\nu+\sigma_\omega\nu_t\right)\frac{\partial \omega}{\partial x_j}\right]}{\partial x_j} \tag{4}$$
$$+2\left(1-F_1\right)\frac{\sigma_\omega}{\omega}\frac{\partial k}{\partial x_j}\frac{\partial \omega}{\partial x_j}$$

The turbulent viscosity is written as:

$$\mu_t=\frac{\rho\alpha_1 k}{\max\left(\alpha_1\omega,SF_2\right)} \tag{5}$$

σ_k and σ_ω represent the turbulent Prandtl numbers for k and ω respectively where:

$$\sigma_k=\frac{1}{\frac{F_1}{\sigma_{k1}}+\frac{\left(1-F_1\right)}{\sigma_{k2}}} \tag{6}$$

$$\sigma_k=\frac{1}{\frac{F_1}{\sigma_{\omega1}}+\frac{\left(1-F_1\right)}{\sigma_{\omega2}}} \tag{7}$$

$$P=\tau_{ij}\frac{\partial \overline{u_i}}{\partial x_j} \tag{8}$$

$$\tau_{ij}=2\mu_t S_{ij}-\frac{2}{3}\rho k\delta_{ij} \tag{9}$$

$$S_{ij}=\frac{1}{2}\left(\frac{\partial \overline{u_i}}{\partial x_j}+\frac{\partial \overline{u_j}}{\partial x_i}\right) \tag{10}$$

where S_{ij} is the strain rate tensor.

F_1 and F_2 are the blending functions which are given by:

$$F_1=\tanh\left\{\left\{\min\left[\max\left(\frac{\sqrt{k}}{\beta\omega y},\frac{500\nu}{y^2\omega}\right),\frac{4\sigma_{\omega2}k}{CD_{k\omega}y^2}\right]\right\}\right\} \tag{11}$$

$$F_2=F_1=\tanh\left\{\left[\max\left(\frac{2\sqrt{k}}{\beta\omega y},\frac{500\nu}{y^2\omega}\right),\frac{4\sigma_{\omega2}k}{CD_{k\omega}y^2}\right]\right\} \tag{12}$$

where $S=\sqrt{2S_{ij}S_{ij}}$ is the strain rate magnitude.

As free stream and inside boundary layer use the different models, all of the constants ϕ are a blend of inner (F_1) and outer (F_2) constants, blended via the following linear equation:

$$\phi=F_1\phi_1+\left(1-F_1\right)\phi_2 \tag{13}$$

The additional equations and constants (Table 1) of the SST model k-ω are also given by:

$$P_k=\min\left(\tau_{ij},\beta^*k\omega\right) \tag{14}$$

$$CD_{k\omega}=\max\left(2\delta\sigma_{\omega2}\frac{2}{\omega}\frac{\partial k}{\partial x_i}\frac{\partial \omega}{\partial x_i},10^{-10}\right) \tag{15}$$

2.2.2 Calculation of Forces and Aerodynamic Coefficients

The blade profile is subdivided into n nonuniform surface elements ds in the computational domain from which the elementary force $\overrightarrow{dF}$ applied on the surface element is written as:

$$\overrightarrow{dF}=-p\vec{n}ds+\tau\vec{t}ds \tag{16}$$

The terms $-p\vec{n}ds$ and $\tau\vec{t}ds$ represent the pressure force and viscous force, respectively. $\vec{n}$ and $\vec{t}$ are the normal and tangential unit vectors to the surface element ds.

The integrated components over the entire blade surface give the axial $\overrightarrow{F_A}$ and normal $\overrightarrow{F_N}$ forces exerting on the blade (Fig. 1).

The resulting force $\vec{F}$ exerting on the blade element is written as:

$$\vec{F}=\overrightarrow{F_A}+\overrightarrow{F_N} \tag{17}$$

The aerodynamic forces such as drag $\overrightarrow{F_D}$ and lift $\overrightarrow{F_L}$ are calculated by projecting the resultant force in the direction of flow ($\overrightarrow{V_\infty}$) and perpendicular to the flow direction, respectively, as mentioned in Fig.1.

$$\overrightarrow{F_D}=\overrightarrow{F_N}\cos\left(\alpha\right)-\overrightarrow{F_A}\sin\left(\alpha\right) \tag{18}$$

$$\overrightarrow{F_L}=\overrightarrow{F_N}\sin\left(\alpha\right)+\overrightarrow{F_A}\cos\left(\alpha\right) \tag{19}$$

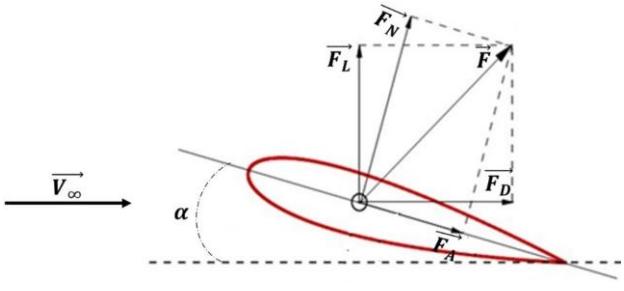

Fig. 1 Aerodynamic forces exerted on a static blade element

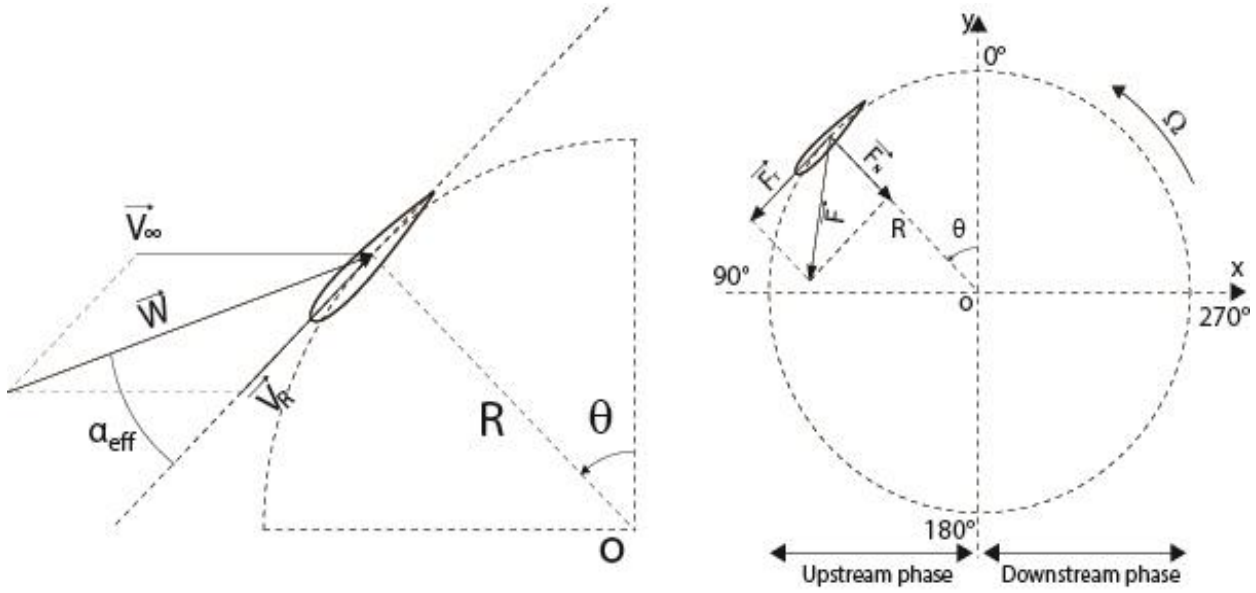

(a) (b)

Fig. 2 Aerodynamic forces exerted on the dynamic blade element

Finally, the output files corresponding to the drag (Eq.20) and lift (Eq.21) coefficients are given as a function of iterations by:

$$C_D = \frac{\left\|\overrightarrow{F_D}\right\|}{\frac{1}{2}\rho V_\infty^2 c} \tag{20}$$

$$C_L = \frac{\left\|\overrightarrow{F_L}\right\|}{\frac{1}{2}\rho V_\infty^2 c} \tag{21}$$

Where, $\frac{1}{2}\rho V_\infty^2 c$ is the dynamic force per width unit.

The physical understanding of the behavior of a Darrieus wind turbine requires kinematic and dynamic analysis of the relative motion of the airflow around a single blade, as shown in Fig.2.

Fig.2a describes the kinematics of the relative airflow around a blade that has a uniform circular motion (counterclockwise) for each TSR. The resultant of the relative wind velocity vector $\vec{W}$ is given as:

$$\overrightarrow{W} = \overrightarrow{V_\infty} - \overrightarrow{V_R} \tag{22}$$

Where $\overrightarrow{V_R}$ is the rotational velocity vector of a single blade.

The effective angle of attack α_{eff} is defined as the angle between the relative wind velocity $\vec{W}$ and the axial direction of the blade element, it's given by:

$$\alpha_{eff} = \tan^{-1}\left[\frac{\sin(\theta)}{\cos(\theta) + TSR}\right] \tag{23}$$

This quantity varies cyclically as a function of the azimuth angle θ and the tip speed ratio (TSR), which is the ratio of the free stream velocity to the rotor speed:

$$TSR = \frac{\Omega R}{V_\infty} \tag{24}$$

The wind turbine is operated by the resultant force $\vec{F}$ generated by the blade which can be decomposed to a tangential $\overrightarrow{F_T}$ and normal $\overrightarrow{F_N}$ components as can be seen on Fig.2b.

$$\overrightarrow{F} = \overrightarrow{F_T} + \overrightarrow{F_N} \tag{25}$$

These components depend directly on the drag force $\overrightarrow{F_D}$, lift force $\overrightarrow{F_L}$ and the effective angle of attack α_{eff} where:

$$\overrightarrow{F_N} = \overrightarrow{F_L}\cos\left(\alpha_{eff}\right) + \overrightarrow{F_D}\sin\left(\alpha_{eff}\right) \tag{26}$$

$$\overrightarrow{F_T} = \overrightarrow{F_L}\sin(\alpha_{eff}) - \overrightarrow{F_D}\cos\left(\alpha_{eff}\right) \tag{27}$$

The torque generated by each blade is defined as the vector product of the radius vector $\vec{R}$ and the resultant force.

$$\overrightarrow{M} = \vec{R} \times \vec{F} \tag{28}$$

Then the module of the torque generated by a single blade is given by:

$$\left\|\overrightarrow{M}\right\| = R\left\|\overrightarrow{F_T}\right\| \tag{29}$$

According to Eq.29 and Eq.27, the torque generation depend directly on the drag $\overrightarrow{F_D}$ and lift $\overrightarrow{F_L}$ forces generated by each blade.

$\overrightarrow{F_L}$ has a positive impact and $\overrightarrow{F_D}$ has a negative effect on the torque generation. However, the improvement in torque generation is achieved by using of a method that enhance $\overrightarrow{F_L}$ and/or reduce $\overrightarrow{F_D}$, thus improving the aerodynamic efficiency of the blade.

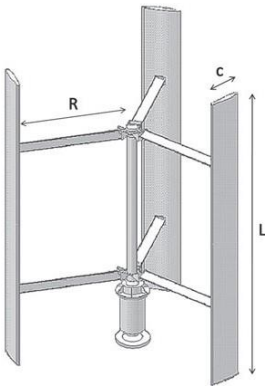

Blade profile	NACA0015 with a rounded trailing edge
Chord length	c=0.4m
Blade spanwise	L=3m
Number of blades	N=3
Radius of turbine	R=1.25m
Blade/shaft connection	Centred shaft (0.5c)

Fig. 3 Schematic straight Darrieus wind turbine with its characteristics

During the rotation of the vertical axis wind turbine, the torque coefficient C_m of the blade varies as a function of the azimuth angle θ and is given by:

$$C_m(\theta) = \frac{\|\vec{M}\|}{\frac{1}{2}\rho A R V_\infty^2} \tag{30}$$

The power curve of a VAWT describes the evolution of the power coefficient C_P as a function of the TSR. C_P is defined as follows:

$$C_P = \frac{1}{2\pi}\int_0^{2\pi}\left[\frac{\Omega\|\vec{M}\|}{\frac{1}{2}\rho A V_\infty^3}\right]d\theta \tag{31}$$

$$C_P = TSR \times \overline{C_m(\theta)} \tag{32}$$

The chord-based Reynolds number is defined as:

$$\mathrm{Re}_c = \frac{\rho V_\infty c}{\mu} \tag{33}$$

2.2.3 Calculation Domain and Mesh Generation

The micro-straight-bladed VAWT model analyzed in our study is the one experimentally tested in the wind tunnel of the National Research Council NRC in Ottawa, Canada by Bravo et al. (2007), whose characteristics are illustrated in Fig.3.

The computational domain design (Fig.4a) was created on the ANSYS/Design Modeler software with the same dimensions as the one created by McLaren et al. (2012). The center of the shaft represent the origin of the domain and it's positioned at a distance of 8R from the inlet, upper and lower faces respectively. The rectangular computational domain of 28R × 16R is divided into two main parts that are the fixed part and the rotating part, separated by a circular interface of 5.6R diameter. The rotating part surrounding the rotor is subdivided, by three interfaces, to four subdomains (Fig. 4b). Three subdomains of diameter 2c surrounding the blades to

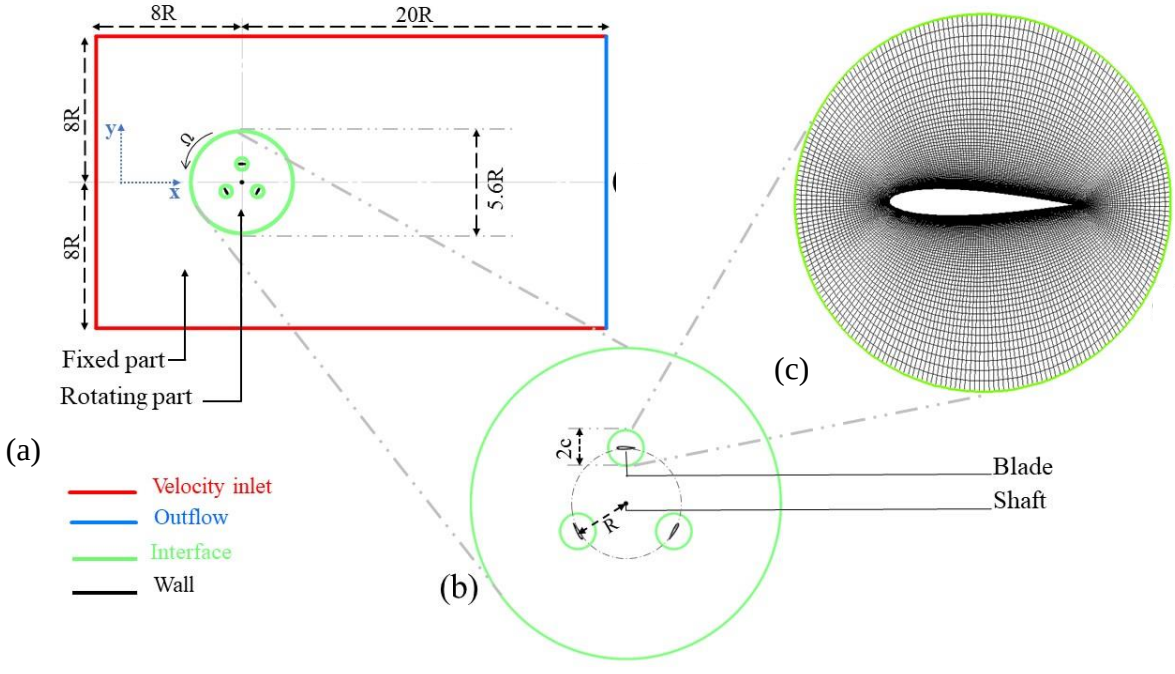

Fig. 4 (a) Calculation domain (b) Rotating part (c) Mesh around blade element

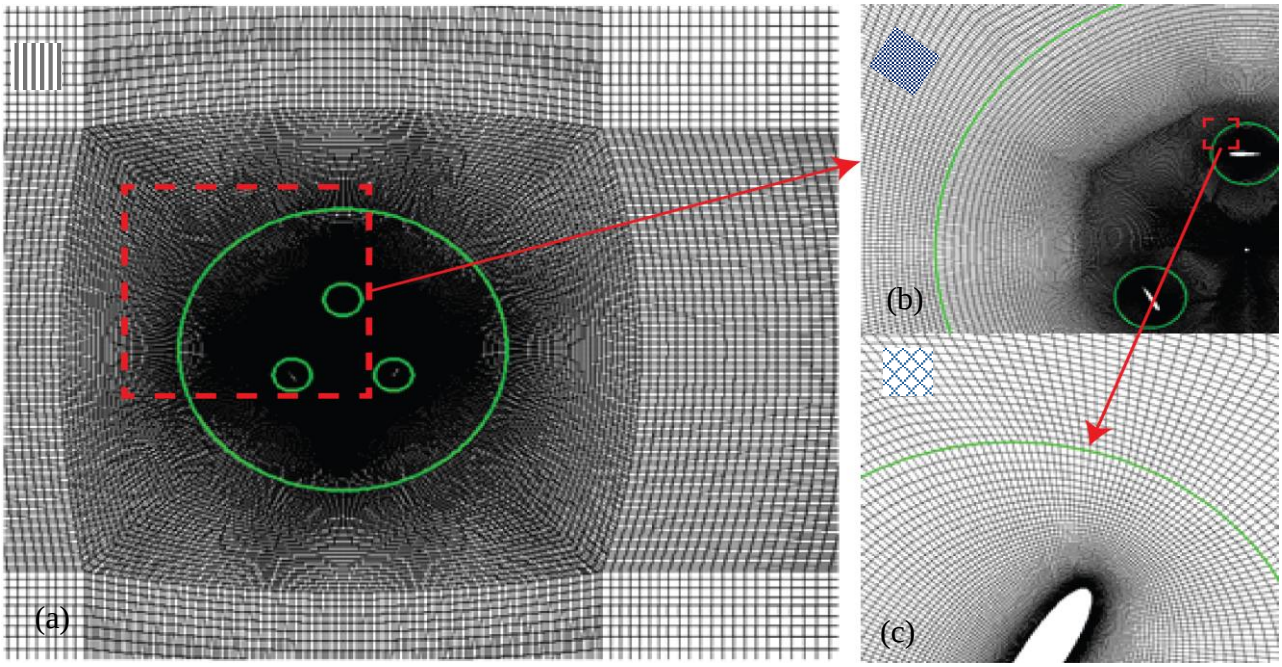

Fig. 5 (a) non-uniform structured mesh generated in the computational domain, (b) and (c) Conformal mesh between two adjacent fluid zones

simplify the pitch control of the blades, and the fourth subdomain includes the three subdomains and the rotor shaft. So, our computational domain contains five fluid zones: a fixed zone and four dynamic zones. The boundary conditions used in our study are shown in Fig. 4.

The non-uniform structured mesh shown in (Fig. 5a) is generated in the computational do main using the multiblock method via ANSYS/ICEM software. The mesh is refined in the near wall (Fig. 4c) to ensure the capture of the high gradients of the turbulent and mean variables of the flow in this region. The diffusion of the information between the five fluid zones is done through the connecting interfaces, so we respected the equality of the cell size at the interfaces between neighbored fluid zones (Fig. 5b and Fig. 5c) to minimize the interpolation error between these zones and avoid vorticity generation.

2.2.4 Boundary Conditions and Solver Settings

The unsteady numerical airflow simulations around the straight bladed VAWT are performed on ANSYS/FLUENT software, calibrated in 2D double precision (2d, dp). The pressure-based were used to establish an incompressible fluid flow with constant physical parameters. The effect of gravity is negligible, and the operational pressure reference (1.013×105 Pa) has been taken at the inlet of the computational domain (x=-8R). The free stream velocity was fixed to V_∞ = 13.45 m/s along the x-direction (Fig. 4a) with 1% turbulent intensity and the turbulence length scale of 0.1c. The gauge pressure is zero and no slip condition is fixed at the walls. The schemes of pressure-velocity correction and space-time discretization are mentioned in Table 2 and the residuals are set to 10^{-5} for all variables.

2.2.5 Grid Independency

The computing station used to realize our simulation has an Intel(R) Core (TM) i7-10700K CPU @ 3.80GHz and 32GB of RAM. Three different size meshes were tested to ensure good accuracy in predicting the aerodynamic coefficients and the power curve (Table 3). The tests were performed on the torque coefficient C_m during a revolution. The time step is equivalent to 2◦ of rotation with 50 iterations by time step. The convergence of the torque coefficient is ensured only at the fifth revolution. For that reason, the results represented in what follows are for the sixth cycle. Figure 6 represents the torque coefficient evolution for the different mesh sizes mentioned in Tab.3 at TSR=1.7. We notice that the C_m evolution estimated by the medium and fine meshes are quite similar, contrary to the considerable difference between the coarse mesh and the other meshes. So, to optimize the computation time and the computer capacities, we opted for the medium mesh in the rest of the calculations. This provided considerable gains: 192750 cells and 53mn 51s by revolution. The correspondent values of y^+_{max} and $\overline{y^+}$ inferior to 5 and 1, respectively, are sufficient to detect physical phenomena in the sub-boundary layer.

Table 2 Methods and spatiotemporal discretization schemes

Pressure-Velocity coupling	PISO
Gradient	Green-Gauss cell based
Pressure	Second Order
Momentum	Second order Upwind
Turbulent Kinetic Energy	Second order Upwind
Specific Dissipation Rate	Second order Upwind
Transient Formulation	Second Order Implicit

2.2.6 Time Step Sensitivity

To ensure that the solver has correctly predicted the flow structure and numerical stability throughout the transient simulations, selecting a suitable time step Δt is

Table 3 Control parameters of different mesh sizes tested

Mesh	Cells number	Elements number around blade	First layer thickness (m)	Growth rate	y^+_{max}	$\overline{y^+}$	Calculation time by cycle
Coarse	60626	120	4×10^{-5}	1.05	5.829	1.561	00h 16mn 33s
Medium	192750	240	1×10^{-5}	1.05	1.708	0.448	00h 53mn 51s
Fine	568800	480	1×10^{-5}	1.05	1.562	0.446	03h 28mn 54s

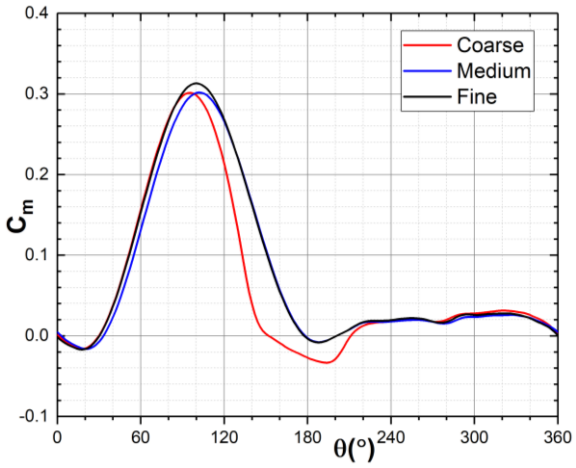

Fig. 6 Torque coefficient for different mesh size at TSR=1.7

essential. In the context of numerical simulations of airflow around SD-VAWT using the sliding-mesh method, it is impossible to establish an optimal time step due to the considerable variation in rotational speed as a function of TSR and the complexity of the flow field. To predict the power coefficient for each TSR, the time step Δt is equivalent to a wind turbine rotation increment Δθ. In this case, the transient numerical simulations were performed with a variable time step from which their calculation was performed as follows:

The wind turbine's rotational speed Ω represents the wind turbine's angular frequency. It defines the trajectory covered by the blade element in one second. It is described in rad/s. The angular frequency is calculated from Eq.24.

$$\Omega = \frac{TSR \times V_\infty}{R} \tag{34}$$

The rotation period T of the blade element can be written as follows:

$$T = \frac{2\pi}{\Omega} \tag{35}$$

T is expressed in seconds, and describes the time required for the blade element to make one complete revolution (360°).

To track the flow structure around the blade element and the interaction wake/blade, we apply the triple rule to calculate the time step corresponding to the increment blade rotation as follow:

$$T(s) \rightarrow 360°$$

$$\Delta t \rightarrow \Delta\theta$$

$$\Delta t = \frac{T \times \Delta\theta}{360} \tag{36}$$

The time step independency analysis based on the average of the torque coefficient $\overline{C_m}$ of the medium mesh (Table 3 And Fig. 6) was performed at 1°, 2°, 5° and 10° increments with a second order implicit transient formulation scheme (Table 2) at TSR=1.7. for the time step convergence criterium, the following equation was used between each two consecutive different time steps:

$$\frac{\left|\Delta\left(\overline{C_m}\right)\right|}{\overline{C_m}} = \frac{\left|\overline{C_{m,new}} - \overline{C_{m,old}}\right|}{\overline{C_{m,new}}} \tag{37}$$

As shown in Table 4, When the time steps reach 0.00190733 (corresponding to Δθ=2°), the average of the torque coefficient $\overline{C_m}$ of a single blade element basically does not change.

2.3 Proposed Passive Control Flow Methods

The variation of the torque generated by the straight Darrieus VAWT as a function of the azimuth angle has a wavy shape due to the cyclical variation of the local angle of attack of the flow, resulting in a complex flow. Optimization of the blade geometry is one of the solutions that allow us to passively control the boundary layer to delay or eliminate the dynamic stall and/or minimize the drag caused by the flow separation from the profile surface at high angles of attack.

Table 4 Comparison of averaged torque coefficient with different time steps at TSR=1.7.

Δt(s)	Δθ(°)	A periodic iterative step	$\overline{C_m}$	$\frac{\left\|\Delta\left(\overline{C_m}\right)\right\|}{\overline{C_m}}$ (%)
0.009536652	10	36	0.05697	-
0.004768326	5	72	0.07955	28.39
0.00190733	2	180	0.07302	08.94
0.00095367	1	360	0.07310	0.11

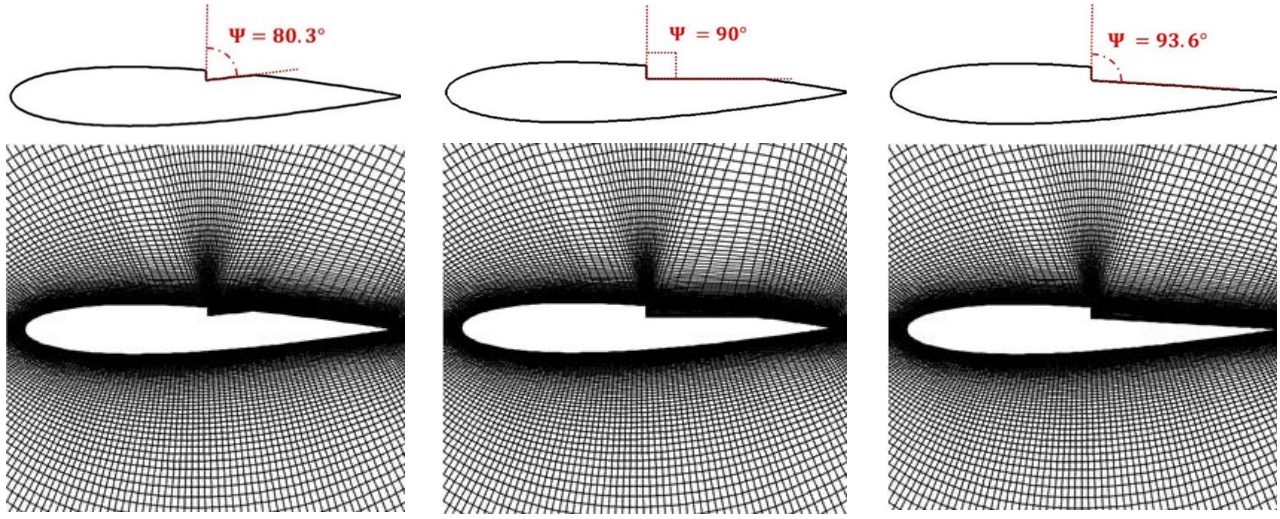

(a) Acute Step Angle (ASA) (b) Right Step Angle (RSA) (c) Obtuse Step Angle (OSA)

Fig. 7 Mesh around different KFA-2 with different opening step angles

Fig. 8 Geometrical presentation of a straight step and a rounded step

In the present work, we are interested in the Kline and Fogleman airfoil (KFA), which was first used in 1968 by Kline and Fogleman to improve the lift and delay the dynamic stall of small scale aircraft (Gross, 2019). This specific airfoil design consists of adding one or more backward steps to the basic profile surface. It is called KFA-1 when the profile has one step on the lower surface, KFA-2 when the step is on the upper surface, KFA-3 when two steps are on the upper surface and, KFA-4 when there are two identical steps, one on the upper surface and the other on the lower surface (Boudis et al., 2018; Kabir et al., 2021). According to the experimental study of Fertis (1986), the KFA-2 design delays or eliminates the dynamic stall of NACA23012, while Frunzulica et al. (2014) confirmed that this design improves the power coefficient of a VAWT profiled by NACA0012. Therefore, we tested three different KFA-2 designs on the conventional NACA0015 profile. The difference is based on the variation of the opening step angle Ψ performed at 50% of the chord with a depth of 25% of the local thickness (Fig. 7). The opening angles Ψ=90◦ and Ψ=93.6◦ were chosen according to the study of Fertis (1986), where they considered a NACA23012 profile. The Ψ=80.3◦ one is performed on the NACA0012 profile by Frunzulica et al. (2014). According to previous studies, symmetrical profiles are better than asymmetrical ones for the operation of SD-VAWT (Danao et al., 2012; Mohamed, 2012). The KFA-2 and KFA-4 designs were then compared for the most optimal angle to obtain a good energy extraction over the entire operating range studied (α^+ and α^-). We then considered a rounded step, which represents a circular arc of diameter D_S, coincident with the top of the step and tangent to the step (Fig. 8). The effect of the diameter D_S on the aerodynamic force was also considered.

3. RESULTS AND DISCUSSION

3.1 Validation

The CFD simulation results are validated against the experimental data published by Sheldahl and Klimas (1981) for a $Re_c=3.68\times10^5$. The distribution of the lift coefficient C_L versus the angle of attack (AoA) α for the conventional static airfoil NACA0015 is shown in Fig. 9a. It can be seen that the RANS SST k-ω model has a good trend, especially for α≤12° with a relative error of less than 13%, and an overestimation of C_L for α>12° with a relative error not exceeding 17% (similarly to results from previous numerical studies (McLaren et al., 2012; Sun et al., 2019). The static stall angle was well captured at an angle of α=14°, offset by 1° from the experiment. This behavior has already been observed by Winslow et al. (2018), Rogowski et al. (2020), and Baxevanou and Fidaros (2008), who showed that 2D RANS models overestimate the performance for relatively high α (relative to the onset of flow separation) due to the following reasons: (1) the 3-D effects, border effects, and wall roughness are negligible, (2) the inability of the 2D RANS models to accurately capture the laminar separation bubble and the position of the flow separation point, (3) the difficulty to accurately capture the experimentally predicted stall angle due to the instability of the flow.

Then, the evolution of the power coefficient versus TSR of the three-bladed VAWT described in Fig. 3 compared with the experimental data of Bravo et al. (2007) and with the numerical results available in the literature are shown in Fig. 9b. The different calculation

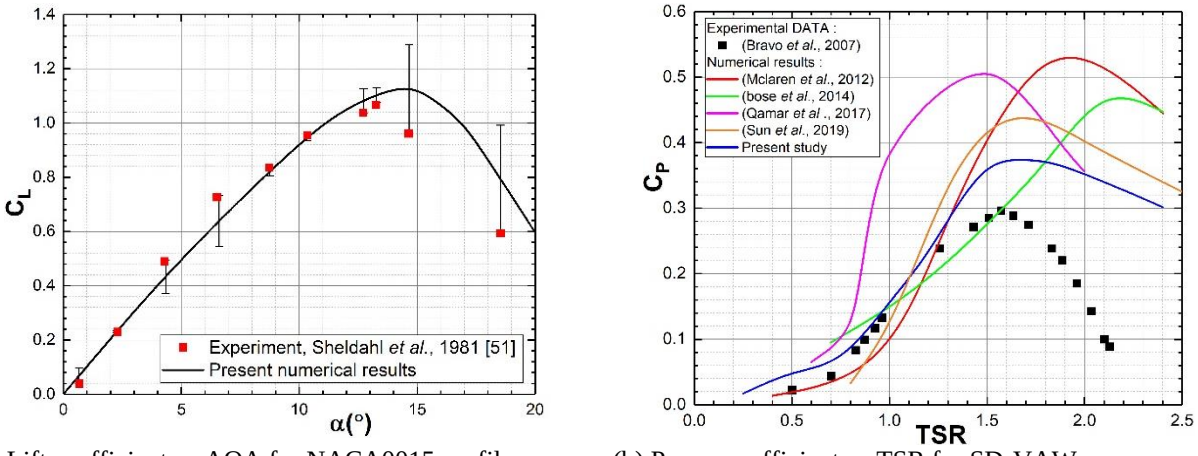

(a) Lift coefficient vs AOA for NACA0015 profile (b) Power coefficient vs TSR for SD-VAW

Fig. 9 Numerical validation results

Table 5 Control parameters of different mesh sizes tested

Authors	Mesh type	Pressure-Velocity Coupling	Fluid zones number	Cells number
(McLaren et al., 2012)	Triangular	SIMPLE	2	485000
(Bose Sumantraa et al., 2014)	Quadratic pave	Coupled	2	157025
(Qamar & Janajreh, 2017)	Quadratic pave	SIMPLE	3	400000
(Sun et al., 2019)	Quadratic pave	Not mentioned	3	200000
Current results	Quadratic map	PISO	5	192750

conditions are summarized in Table 5. Overall, the 2D URANS SST k-ω turbulent model overestimates the prediction of the power coefficient vs TSR. Fully turbulent URANS models face challenges in accurately predicting stall phenomena, often resulting in overestimation of power output. These models rely on averaged quantities, which can introduce inaccuracies in complex flow fields typical of Darrieus wind turbines. Additionally, their effectiveness diminishes at high Reynolds numbers, presenting further issues for turbines operating at high TSR (Lanzafame et al., 2014; Rezaeiha et al., 2019; Lanzafame et al., 2020). However, compared to the numerical models mentioned in Table 5, our present results have a better prediction of the power curve and the TSR corresponding to the nominal power. This indicates that the non-uniform mapped mesh has a good capability to predict the dynamic flow field around the straight VAWT compared to the triangular and quadratic pave meshes with a reduced computational time.

The current study provides the closest prediction of Cp, with minimal Mean Bias Error (MBE) and Root Mean Square Error (RMSE) values of 9.19 x 10^{-2} and 11.19 x 10^{-2}, respectively. Compared to the literature, numerical predictions from Sun et al. (2019), Qamar and Janajreh (2017), and McLaren et al. (2012) had MBE and RMSE values of 14.63 x 10^{-2}, 15.67 x 10^{-2}, and 16.15 x 10^{-2}, as well as 17.05 x 10^{-2}, 15.87 x 10^{-2}, and 21.66 x 10^{-2}, respectively. In the case of Bose Sumantraa et al. (2014), their results showed MBE and RMSE values of 10.81 x 10^{-2} and 16.29 x 10^{-2}, respectively. Despite seemingly better MBE and RMSE values than other studies from the literature, Bose Sumantraa et al. (2014) were ranked last due to a substantial rightward shift in the power curve resulting from a significant overestimation of the TSR corresponding to the nominal power. This shift becomes evident when aligning the TSR corresponding to $C_{p,max}$ (around 2. for the present study.25) with that reported by Bravo et al. (2007), (1.57), revealing the clear overestimation of the power curve, as already indicated by the overestimation of $C_{p,max}$. The respective MBE and Mean Relative Error (MRE) for predicting the TSR corresponding to nominal power were 12.73 x 10^{-2} and 7.49% for the present study, respectively. While Qamar and Janajreh (2017) had values of 7.27 x 10^{-2} and 4.85%, Sun et al. (2019) had 11.64 x 10^{-2} and 7.39%, McLaren et al. (2012) had 36.25 x 10^{-2} and 18.73%, while Bose Sumantraa et al. (2014) reported 64.12 x 10^{-2} and 28.96% for MBE and MRE, respectively. It is important to note that although Qamar and Janajreh (2017) had a more accurate prediction of TSR corresponding to $Cp_{,max}$, they significantly overestimated $C_{p,max}$ and the entire power curve. Overall, a good power curve estimation should be assessed by accurately predicting both the TSR corresponding to $C_{p,max}$, and estimating the power coefficient. From the beforehand statistical analysis, it can be concluded that the present study is, overall, more accurate than previous numerical studies with identical straight Darrieus wind turbine prototype, boundary conditions, and turbulence model (SST k-ω).

The challenges in numerical simulations for straight Darrieus VAWTs stem from employing a variable time step (for each TSR) to construct the power curve, as well as the significant fluctuation of the cell convective Courant number near the wall due to the dynamic mesh utilized in our simulations. This suggests that information travels through the cell faster than the grid resolution can handle, resulting in numerical instability. The "Coupled" and "SIMPLE" (Semi-Implicit Method for Pressure-Linked Equations) algorithms exhibit limited precision in capturing the flow dynamics due to the inherent instability

in their calculations. Consequently, the power curves derived from previous numerical studies were offset in terms of predicting the TSR corresponding to the nominal power. We have employed the Pressure-Implicit with Splitting of Operators (PISO) pressure-velocity coupling scheme to address this issue and ensure accurate solution predictions. This algorithm is an enhancement of the SIMPLE method. It incorporates two crucial corrections: the neighbor correction, aimed at rectifying momentum and preventing high convective Courant numbers, and the skewness correction, facilitating solution convergence on a highly skewed mesh within a comparable number of iterations to that of a more orthogonal mesh (Lanzafame et al., 2014; Li et al., 2023).

3.2 Aerodynamic Efficiency of the Static Blade in Different Kline and Fogleman Airfoil Design

3.2.1 Effect of the Opening Step Angle on the Straight KFA-2

The 2nd and 4th Kline and Fogleman models are designed on a basic NACA00015 profile to test their aerodynamic efficiency in a static condition. The numerical study was conducted while comparing three geometric modifications of KFA-2 with a straight step as described in Fig. 7.

The evolution of the drag coefficients of the basic profile NACA0015 and the three KFA 2 profiles are shown in Fig. 10. It can be seen that C_D ($|\alpha|$) increases until it reaches a maximum value $C_{D,max}$=0.246 corresponding to $\alpha=\pm15°$, then it decreases until it reaches the negative value C_D =−0.035 at $\alpha=\pm20°$.

All the three KFA-2 modifications allow a reduced C_D compared to the baseline design in the whole α range, except for the OSA design (Ψ=93.6°), which has an excess drag $-14°<\alpha<0°$. Moreover, the reduction rate of the drag coefficient in the range of α^+ is significant compared to that of α^-.

Compared to NACA0015, the OSA design is globally advantageous for drag reduction in the α^+ range, and ASA design is advantageous for the α^- range.

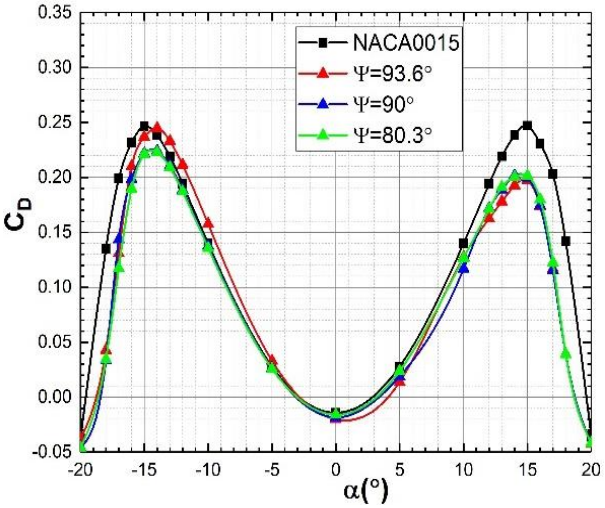

Fig. 10 Effect of the opening step angle on the drag coefficient of KFA-2 design

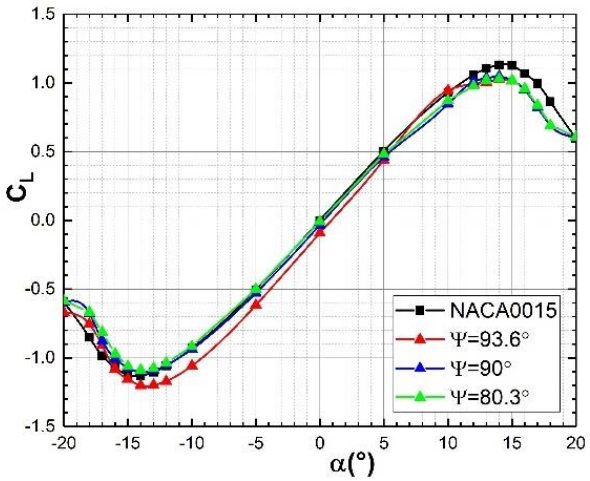

Fig. 11 Effect of the opening step angle on the lift coefficient of KFA-2 design

The |CL (α)| increases until it reaches the maximum value $|C_{L,max}|$=1.13 at $\alpha=\pm14°$ which corresponds to the static stall, then followed by a decrease in $|C_L|$ until it reaches the value 0.597 for $\alpha = 20°$.

For the different other configurations with the straight KFA-2 step, except for the obtuse angle, the numerical results of $C_L(\alpha)$ show a reduction of $|C_L|$ in the whole range of AoA. Compared to NACA0015, the C_L magnitude for Ψ=93.6° case increases for the range $15°<\alpha<0°$ and reaches a better $C_{L,max}$, which corresponds to 6.2% for $\alpha=-14°$.

However, in the α^+ range, the conventional NACA0015 profile is more advantageous. Depending on the operating range α, the analysis of the aerodynamic coefficients of the basic profile and the three modified profiles (KFA-2 opening step angles) shows that some of them are advantageous in C_D reduction and others in lift generation C_L.

In order to select the optimum profile among the four configurations, the distribution of the aerodynamic efficiency C_L/C_D as a function of α is shown in Fig.12.

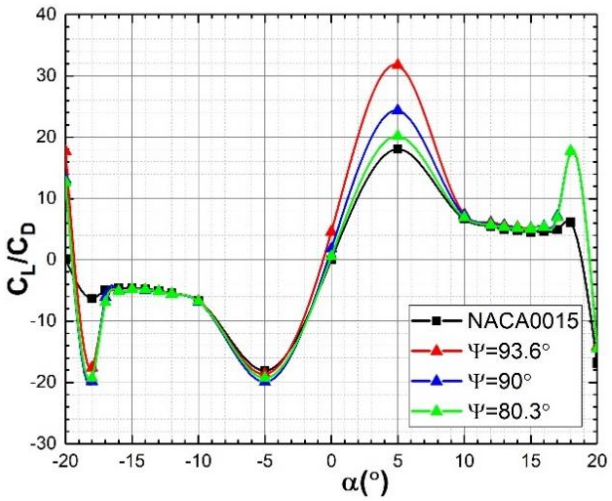

Fig. 12 Effect of the opening step angle on the aerodynamic efficiency of KFA-2 design

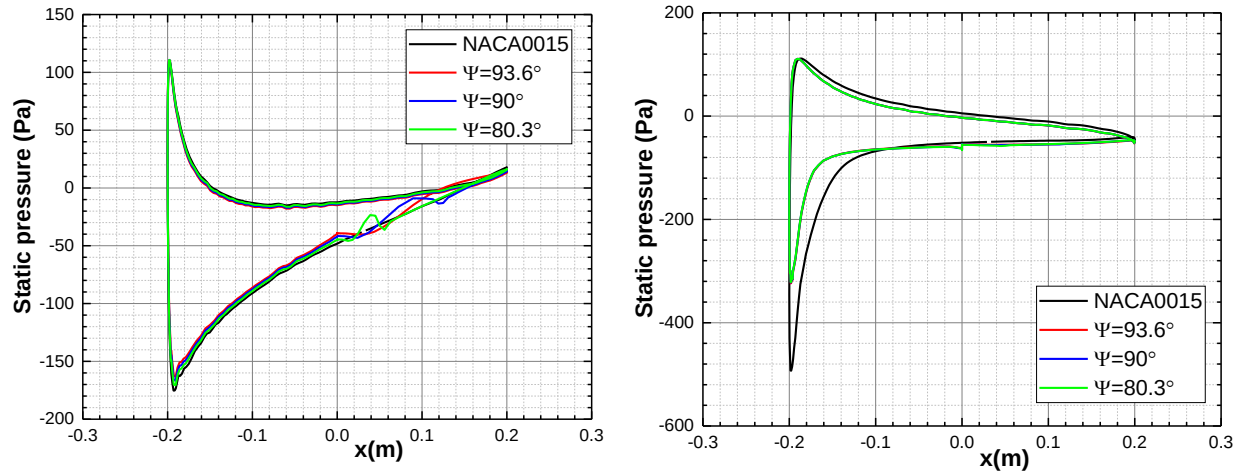

a) α=5° b) α=18°

Fig. 13 Effect of the opening step angle on the static pressure distribution

The aerodynamic fineness of the NACA0015 profile varies oddly C_L/C_D (α) = − C_L/C_D(−α). The absolute value C_L/C_D(α) increases until it reaches the maximum value of 18.05 at α = 5°, then decreases slightly for 5°≤|α|≤17°, followed by a small peak at α=18°, and finally, it decreases until the value -16.86 at α=±20°.

Analysis of the lift-to-drag rate (C_L/C_D) evolution as a function of α reveals that the KFA 2 design has significantly improved the aerodynamic performance of the baseline NACA0015 profile. The maximum aerodynamic efficiency increases as a function of the straight step inclination Ψ. Specifically, Ψ=93.6° represents the best inclination for energy extraction where $(C_L/C_D)_{,max}$=31.74 was obtained at α=±5°, representing a 75.84% improvement over the baseline profile.

Analysis of Fig. 10, Fig. 11, and Fig. 12 suggests that a straight KFA-2 design at mid-chord with a depth of 25% has a good improvement of the aerodynamic performance in the α^+ range. Moreover, straight steps with an inclination Ψ≤90° are favorable in terms of drag reduction, and ~~the~~ inclinations Ψ>90° are also beneficial for lift generation.

The opening step angle has a direct effect on the distribution of the static pressure along the blade profile surface. As can be observed from Fig.12, the effect of the opening step angle is evident for AOA values of ±5° and ±18°, where we, thus, analyze the distribution of the static pressure along the blade profile (Fig.13, α=±5° and α=±18° corresponding to the maximum aerodynamic efficiency and the fully stalled profiles respectively). The difference in static pressure between the top and bottom surfaces decreases as opening step angle increases, reflecting a drop in the lift coefficient compared to the baseline profile. Similarly, the static pressure difference between the leading edge and trailing edge is inversely proportional to the opening step angle, characterizing a decrease in the pressure drag (form drag) compared to the reference NACA0015. For better aerodynamic performance, a higher lift-to-drag ratio is desired. In other words, the rate of decrease of pressure drag must be higher than that of the lift. Furthermore, at α=18° (fully stalled flow), the opening step angle has no effect on the static pressure distribution and thus does not affect the aerodynamic coefficients.

Figure 14 shows the streamlines and pressure distribution contours at two specific AoA: α=5° and α=18° for the standard NACA-0015 and the optimized airfoils. It can be seen that at the smallest angle of attack, the pressure distributions are almost identical for all configurations. Considering the KFA design modification as a vortex generation technique for passive flow control, it is noticeable that a primary vortex has been generated at the corner of the step, which causes the generation of a secondary vortex with a size proportional to the opening step angle. This results in the acceleration of stagnant small vortex sizes at the profile surface, thus reducing drag and improving aerodynamic efficiency.

At an angle of attack of α=18°, the flow is detached from the leading edge, creating two counter-rotating recirculation zones over almost the entire upper surface of the profile. The size of the two counter-rotating zones is proportional to the opening step angle. It should also be noted that the significant inertia of these zones prevents the formation of secondary vortices. Furthermore, in the case of KFA-2, the negative pressure gradient near the leading edge is significantly reduced due to the flow aspiration phenomena downstream of the step. Consequently, the aerodynamic efficiency is improved, which confirms the results of Wang *et al.* (2017). Also, interestingly, even though the modified profiles have larger recirculation zones than the baseline profile, the average drag generated by the modified profiles is lower. This is due to the fact that the reduction in pressure drag (shape drag) is more important than the generation of the induced drag (viscous drag) due to the recirculation zone.

3.2.2 Aerodynamic Characteristics of the KFA-2 and KFA-4 Designs

Since the relative angle of attack variation applied to a wind turbine blade changes cyclically during a rotation, it is necessary to have a modification that improves C_L/C_D in both the α^+ and α^- ranges. In this context, two kinds of design on the basic profile NACA0015 were performed with an inclination of Ψ=93.6° to have a good energy

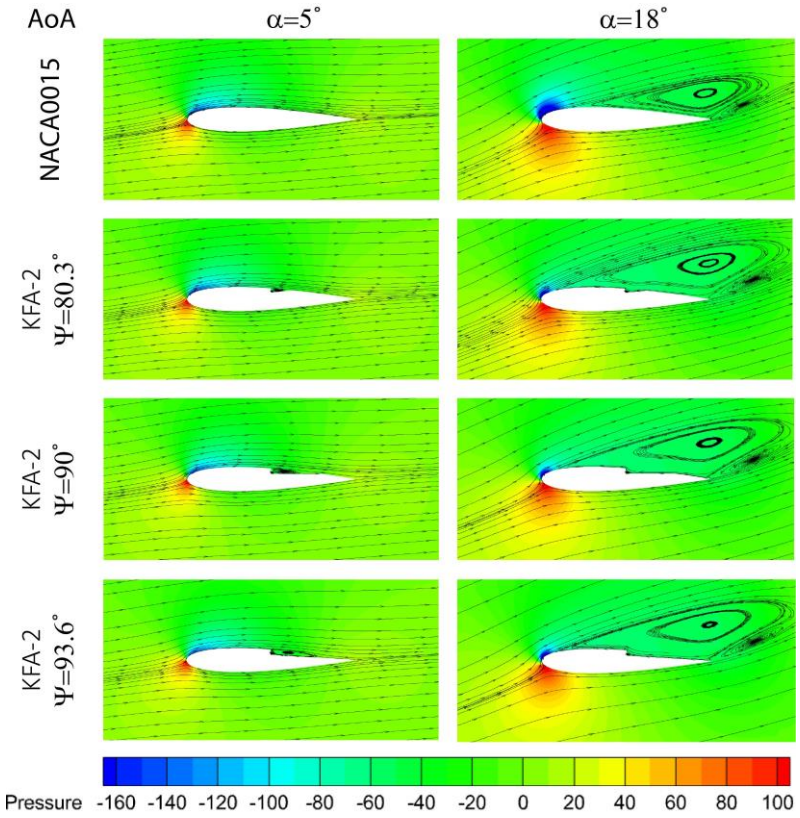

Fig. 14 Effect of the opening step angle on the pressure and streamline distribution

(a) OSA KFA-2 (b) OSA KFA-4

Fig. 15 Geometrical representation of the straight KFA-2 and KFA-4 configurations

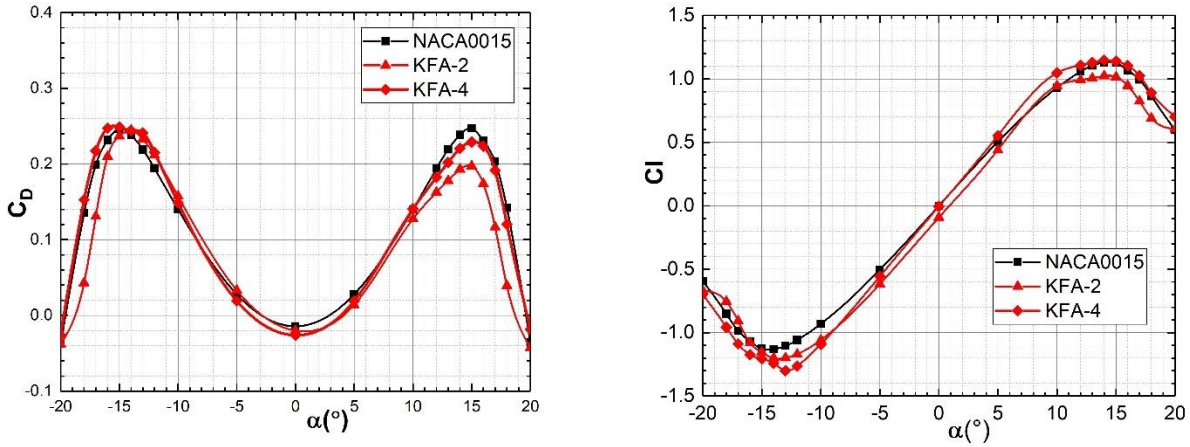

(a) (b)

Fig. 16 Aerodynamic coefficients of OSA KFA-2 and OSA KFA-4 profiles with an opening step angle Ψ=93.6°

extraction at the start of the wind turbine. The geometric configurations specified for KFA-2 and KFA-4 are shown in Fig. 15.

Figure 16a, b, and Fig. 17 show the comparative evolution of the aerodynamic coefficients C_D, C_L, and C_L/C_D for the baseline profile NACA0015 and the two straight profile configurations of the KFA-2 and KFA-4.

The KFA-4 profile has a reduced drag for $\alpha \geq -9°$ and an excess for $\alpha \leq -9°$ with a 7.28% reduction in $C_{D,max}$ at $\alpha=15°$ compared to the baseline profile. On the other hand, KFA-4 has a better lift generation in all the studied operating zone with a maximum excess of 15.15% compared to the NACA0015 profile.

The analysis of the aerodynamic performance can suggest the most optimal configuration that has the potential to improve the self-start and/or the power coefficient of the VAWT prototype studied: KFA-2 has good performance in the α^+ range, and the KFA-4 is favorable in the α^- range. Overall, KFA-4 performs better

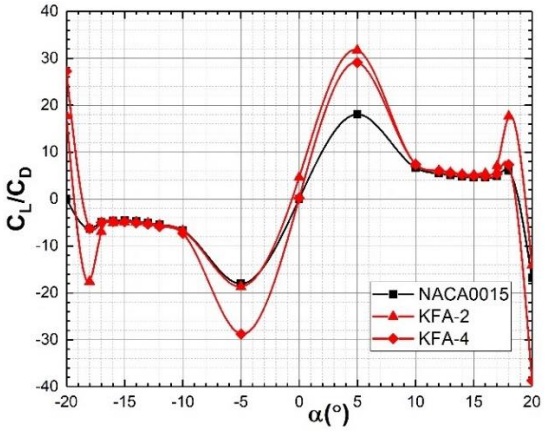

Fig. 17 Aerodynamic efficiency of KFA-2 and KFA-4 profiles

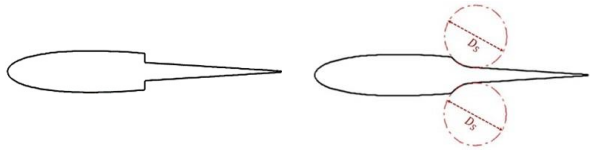

(a) Straight KFA-4 (b) Rounded KFA-4

Fig. 18 Schematic of the rounded and straight KFA-4 configurations

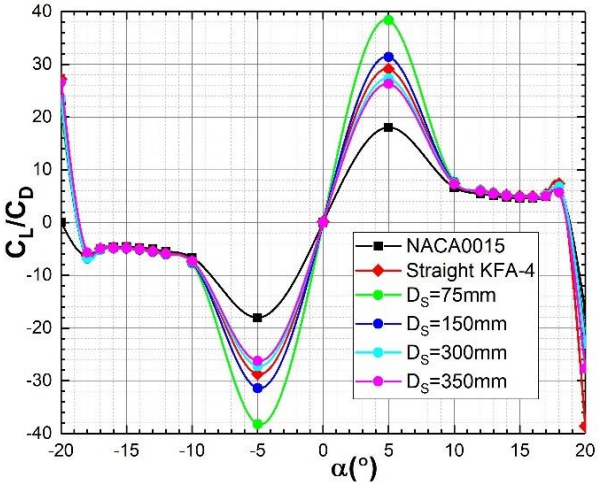

Fig. 19 Effect of diameter curvature on the aerodynamic of rounded KFA-4 profile with an opening step angle Ψ=93.6°

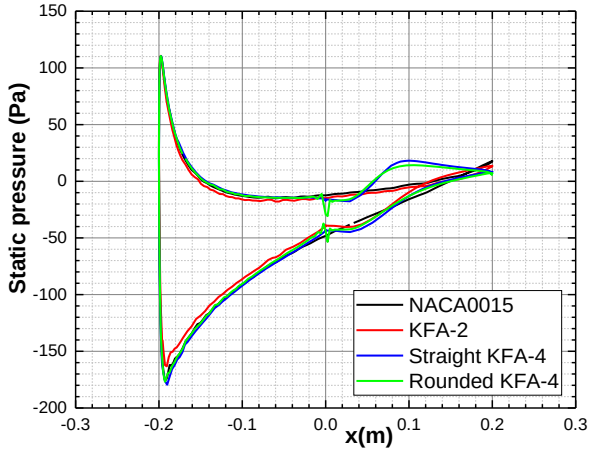

(a) α=5°

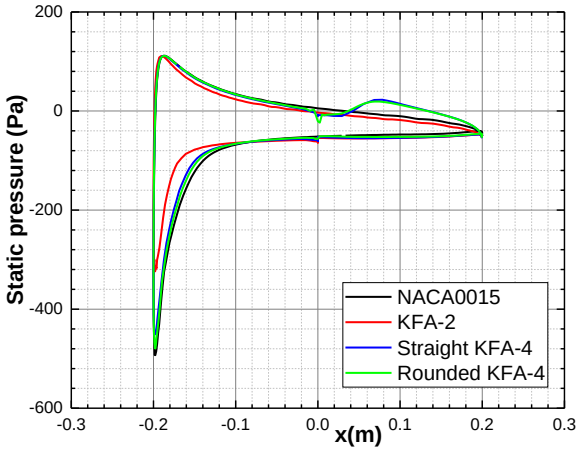

(b) α=18°

Fig. 20 Effect of the KFA modification type and step's geometric shape

than all ~~of~~ the studied geometries thanks to its maximum improvement of 56.94% compared to the baseline design at α=±5°.

3.2.3 Effect of the Step Geometric Shape on the KFA-4 Configuration

As seen previously, the straight KFA-4 design with an inclination Ψ=93.6° is more beneficial for the energy extraction for −10°≤α≤+10°. In this section, we focus on the effect of the step geometric shape on the performance of the modified KFA-4 profile. A straight step is transformed into a rounded step through a circular arc with a diameter D_S coinciding with the edge of the step and tangent to its bottom wall. This operation is carried out on both the airfoil's intrados and extrados, as shown in Fig. 18. The geometry of the blade configuration must be carefully considered to ensure that it can generate more lift without adding too much drag in order to maintain a higher lift-to-drag ratio.

The evolution of the aerodynamic efficiency of the different curvature diameters is shown in Fig. 19. It can be seen that the aerodynamic efficiency decreases as a function of the D_S, which means that the rate of increase of the C_D is higher than that of the C_L. Among the tested cases, a rounded step with a diameter of D_S=75mm is the best one.

In Fig. 20, the distribution of the static pressure along the blade profile designed by different KFA modifications is shown. Unlike the KFA-2 design, the straight and rounded KFA-4 designs resulted in a greater static pressure difference between the upper and lower surfaces resulting in a lift enhancement compared to the reference blade airfoil, especially for the straight KFA-4 design. In terms of the drag coefficient, however, the KFA-2 design reduces the pressure difference between the leading and the trailing edges, thus decreased the drag more than designs compared to the baseline profile. Overall, at AOAs of 5° and 18°, the KFA-2 design reduces the drag more than the KFA-4 and enhances the lift; thus, the KFA-2 improves the aerodynamic performance.

The characteristics of the flow around the rounded KFA-4 with DS=75 mm curvature diameter compared to the straight profile are obtained from the pressure distribution and the streamlines (Fig. 21). Similar to the

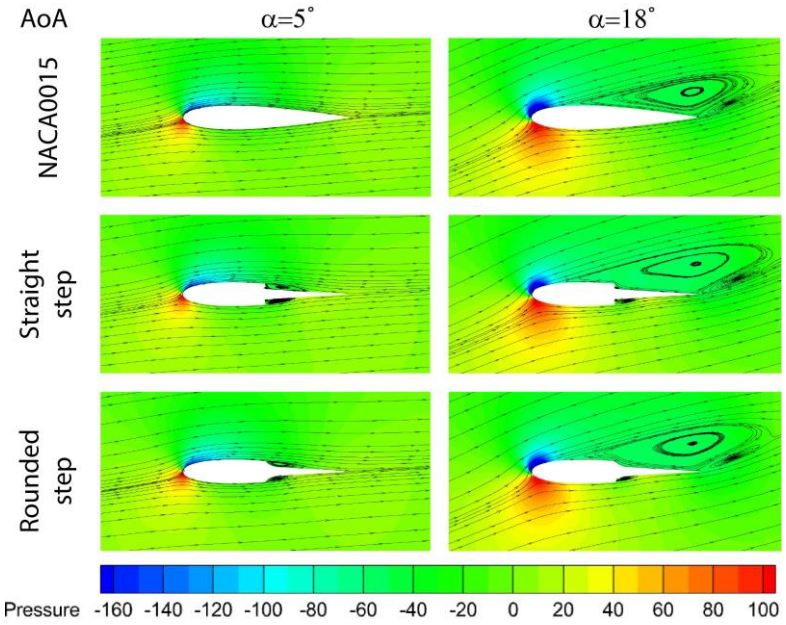

Fig. 21 Pressure and streamline distribution around the KFA-4 configurations

KFA-2 design, the flow does not detach from the KFA-4 and the pressure distributions are almost identical, especially at the leading edge. However, the difference between the rounded and straight steps is noticeable downstream of the steps. Like the straight KFA-2, the straight KFA-4 generates two vortices (primary and secondary), but the rounded KFA-4 generates only the primary vortex. The common vortex is the secondary one in the case of the straight KFA-2 and FKA-4 profiles. In contrast, the primary vortex is not generated in the case of the rounded KFA-4 due to the absence of the flow stagnation that occurs in the corner of the straight steps, which results in a reduction of the induced drag for the rounded KFA-4, improving overall aerodynamic efficiency.

At α=18°, the different KFA-4 profiles are also fully stalled, with the presence of two counter-rotating recirculation zones over most of the upper surface, like the KFA-2 profile. Similarly, to the low angle of attack (α=5°), the rounded KFA-4 prevents the formation of the primary vortex on both the lower and upper surfaces, while the important inertia of the recirculation zones prevents the formation of the vortex downstream of the rounded step of the upper surface. As for the static pressure, the flow aspiration phenomena occur on both surfaces with a slight superiority to the upper surface of the straight and rounded KFA-4, which explains the slight efficiency improvement of the aerodynamic efficiency when compared to the KFA-2 where the greater improvement is due to the absence of the flow separation on the lower surface, leading to a much less important negative pressure gradient.

3.3 Flow Structure Around Dynamic Blades

3.3.1 Aerodynamic Coefficient Analysis of the Basic VAWT

According to Eq.32, the power coefficient C_P depends on the torque coefficient $C_m(\theta)$ generated by the wind turbine blades during one rotation. The evolution of $C_m(\theta)$ at TSR=1.6 is shown in Fig. 22. We can see that the three blades have a similar curve of $C_m(\theta)$ with a phase shift of 120◦ (2π/3 (rad)) between each two successive blades and a slight gap due to the interaction of the vortex structures with the blades. It is easy to see that a blade has a high C_m generation upstream of the cycle (0°≤θ≤180°) and a low torque generation downstream (180°≤θ≤360°). The torque generated by the wind turbine is equal to the sum of the torques generated by the three blades, so in this case, it is possible to get an idea of the torque generated by the turbine from that of a single blade. The global torque generated by a three-bladed wind turbine has a wavy curve with three peaks with a phase shift of 120° (2π/3 (rad)) between each two successive peaks.

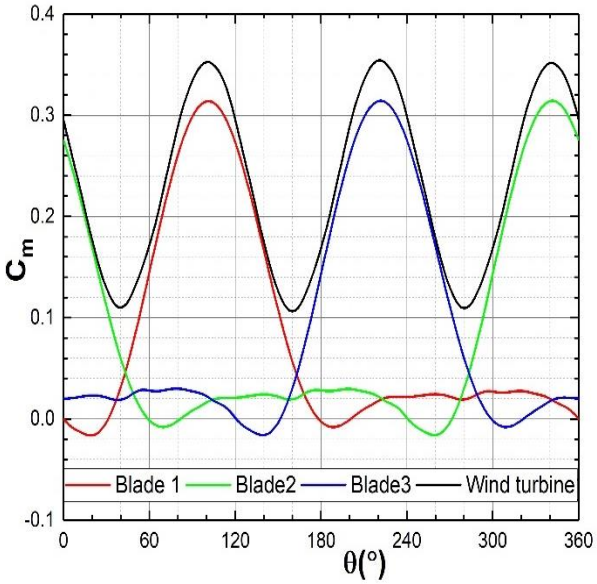

Fig. 22 Torque coefficient for each of the three blades and the wind turbine at TSR=1.6

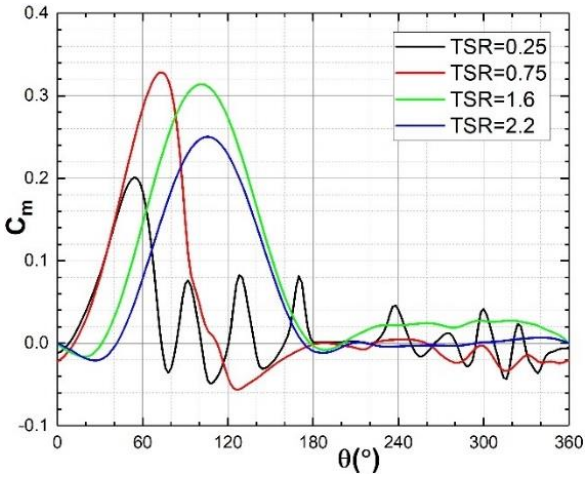

Fig. 23 Torque coefficient of a single blade for different TSR

The evolution of $C_m(\theta)$ of a single blade at different TSRs is shown in Fig. 23. This quantity presents a significant variation in the beginning of the cycle ($0°\leq\theta\leq180°$) where $C_m(\theta)$ increases until it reaches a maximum value corresponding to the torque stall and then decreases. The duration of the torque generation, the value and the position of the maximum torque stall are highly dependent on the TSR. At low TSRs, according to Eq.23 the effective angle of attack varies rapidly leading to a rapid dynamic stall and a drastic decrease in the torque coefficient. The negative value of the C_m at $\theta=0°$ could also explain the inability of the blade to self-start. When the TSR increases, we can see the delay in the torque stall and the increase of the torque generation bandwidth up to TSR=1.6. Beyond this value, the blade speed becomes higher, and the torque generation bandwidth decreases. And therefore, the power coefficient.

In order to better understand the phenomena involved, we present in Fig. 24 for different TSRs (TSR=0.25, 0.75, 1.6, and 2.2) the z-vorticity iso-contours around the blades at different azimuth angle positions ($\theta=0°,30°,50°,90°$).

At low TSR, the high increase in the relative angle of attack, exceeding the dynamic stall value, leads to the separation of the flow from the blade surface and the generation of vortices at the upstream phase of blade 1. The detached vortices will interact directly with the motion of other blades subjected to the dynamic stall in the downstream phase. In this case, the generation of the induced drag will be dominant, resulting in low power. Increasing the TSR results in both a decrease in the relative angle of attack and an increase in the relative wind velocity. At this point, the inertial forces become more dominant than the viscous forces, resulting in a decrease in vortex detachment.

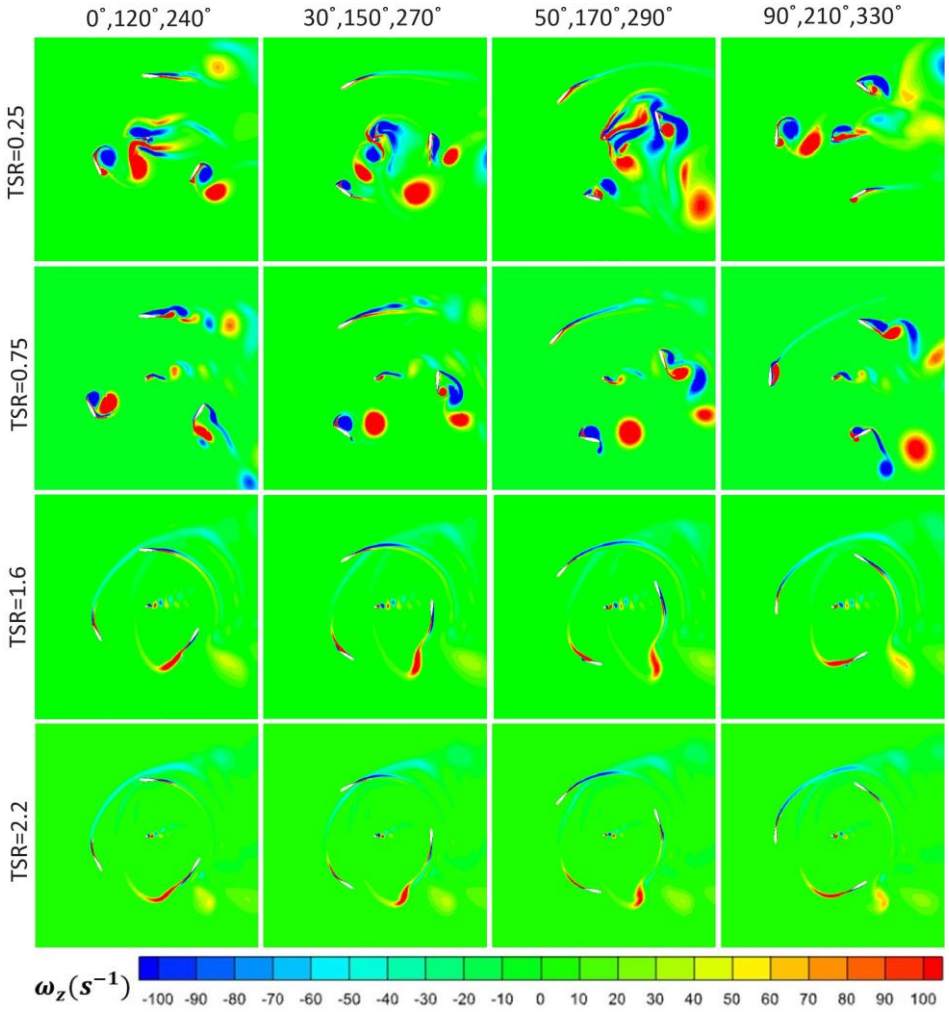

Fig. 24 z-vorticity around the basic wind turbine prototype for different azimuthal position and different TSR

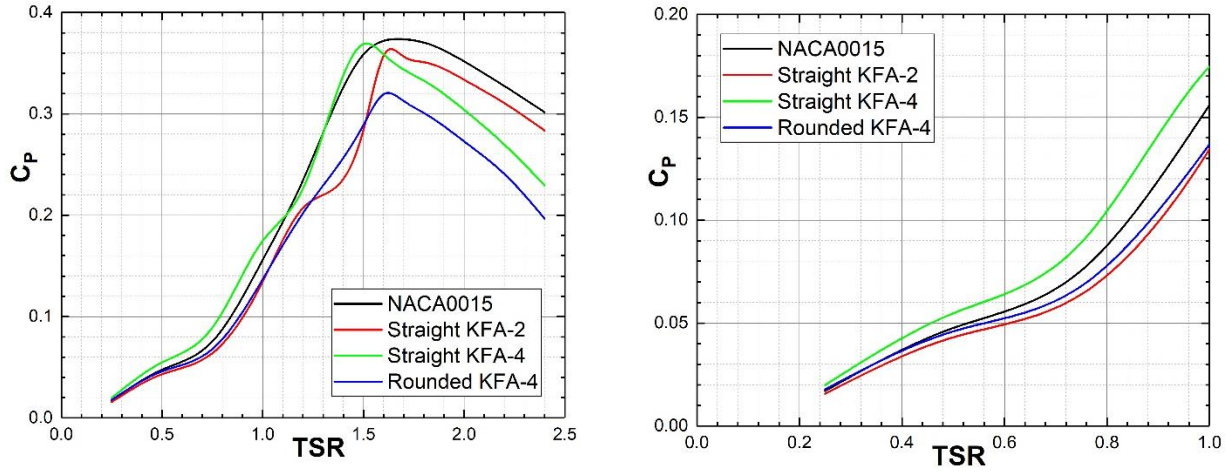

(a) (b)

Fig. 25 Power Coefficient vs TSR for different KFA configurations

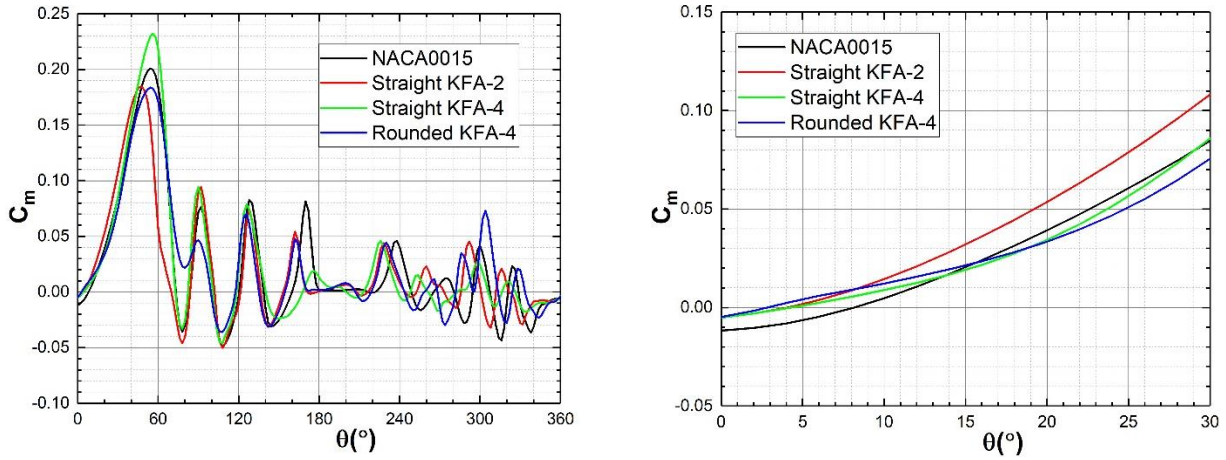

(a) (b)

Fig. 26 Torque coefficient for different KFA design at TSR=0.25

Beyond TSR = 1.6, although the relative angle of attack is low, the Reynolds number is high, and the local torque stall is delayed, the torque generation bandwidth decreases, and consequently, so does the power coefficient. This is because the blade/vortex interaction is more dominant in the upstream phase, and small vortex structures are trapped inside the rotor due to the high rotational speed of the wind turbine. These results are in agreement with the work of Amet et al. (2009).

3.3.2 Effect of the Optimized Blade Profile on the Straight Darrieus VAWT Operating Range

In order to evaluate the most suitable modification for the prototype response, the comparison of the power curve of the turbine with a basic profile NACA0015, KFA-2 with straight step, and KFA-4 with straight and rounded step with a bottom wall inclination Ψ = 93.6 ◦ is shown in Fig. 25. We can see that KFA-2 with a straight step and KFA-4 with a rounded step (DS = 75mm of diameter) are disadvantageous over the whole range of studied TSR. On the other hand, the KFA-4 modification with a straight step is favorable for a low tip speed ratio (TSR=1.6). Notably, the nominal power is also reduced by 1.22%, and the corresponding TSR (TSR=1.5) is lower than that of the basic configuration NACA0015 (TSR=1.7). The power curves of the straight KFA-2 and KFA-4 configurations confirm that symmetrical profiles are recommended for the operation of vertical axis wind turbines.

The torque coefficient distribution of blade 1 at TSR=0.25 for the basic profile and the different modifications is shown in Fig. 26. At the beginning of the cycle (θ=0°), the blade produces a negative torque which refers to the inability of the rotor to self-start. All three modified designs show a good improvement in starting torque compared to the NACA0015 profile. The straight stepped KFA-4 blade allows a better starting torque which is improved by 56% and the maximum torque was captured at θ=55° which reaches an excess of 15.58% compared to the basic geometry.

Therefore, the straight KFA-4 design with a bottom wall inclination of Ψ=93.6° has a positive effect on the operation of the wind turbine, reducing the dead zone and the TSR corresponding to the nominal power and improving the starting torque. However, this design remains unfavorable for high TSR (>1.6).

The results obtained above on the static blade show that the KFA-4 design with a rounded step (DS = 75mm) has a good aerodynamic efficiency compared to the one with a straight step (Fig. 19). However, the test of these

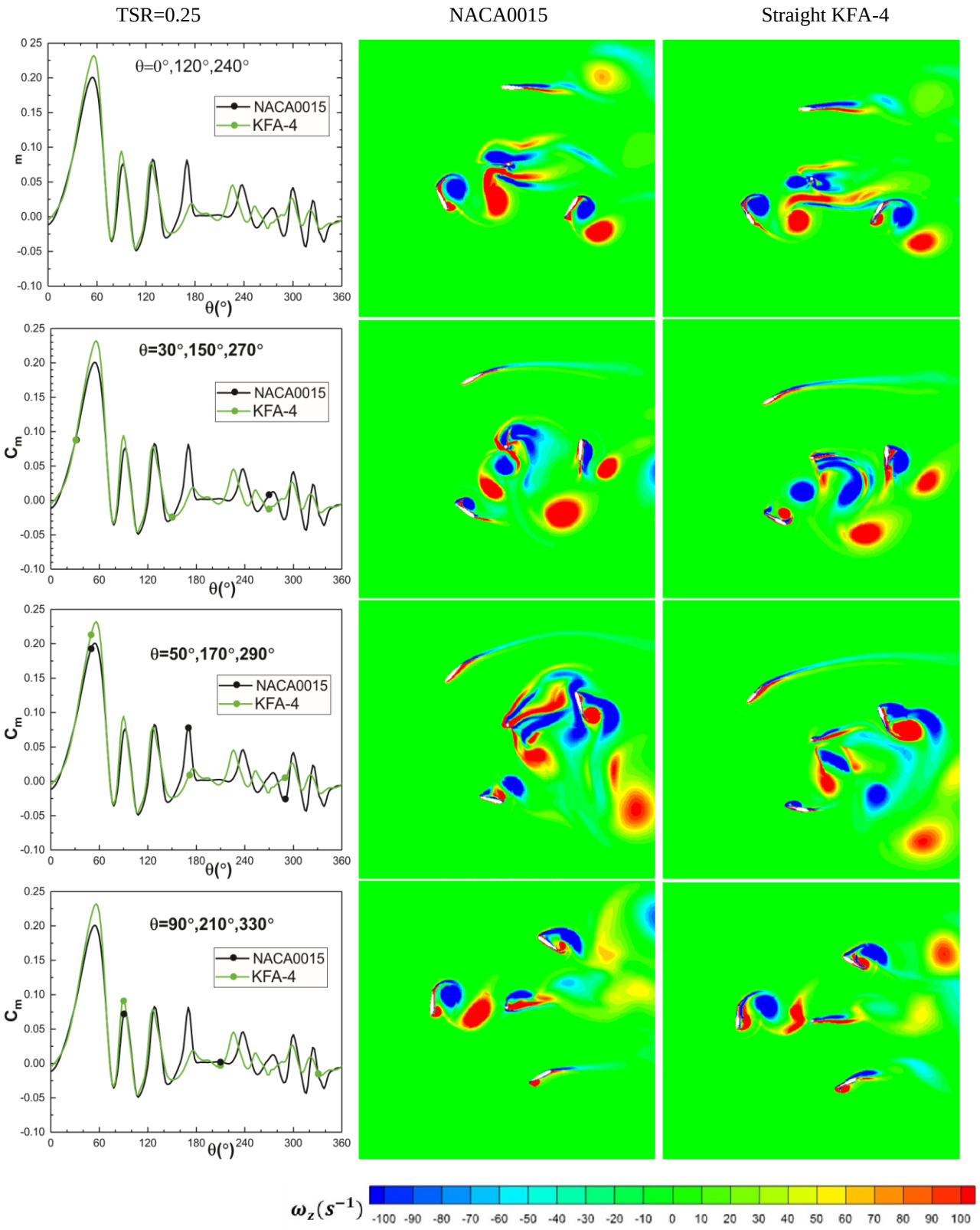

Fig. 27 torque coefficient and z-vorticity around baseline profile and straight KFA-4 design for different azimuthal positions at TSR=0.25

optimized profiles on a three-blade turbine, shows that the straight KFA-4 design is more advantageous for power generation than the rounded one (Fig.25 and Fig.26). The flow around the dynamic blades is indeed more complex, depending on the cyclic variation of the relative angle of attack and the relative wind velocity. The stall pressure point (maximum static pressure), which corresponds to the zero local air velocity, moves rapidly along the dynamic profile as the wind turbine rotates, making it difficult to

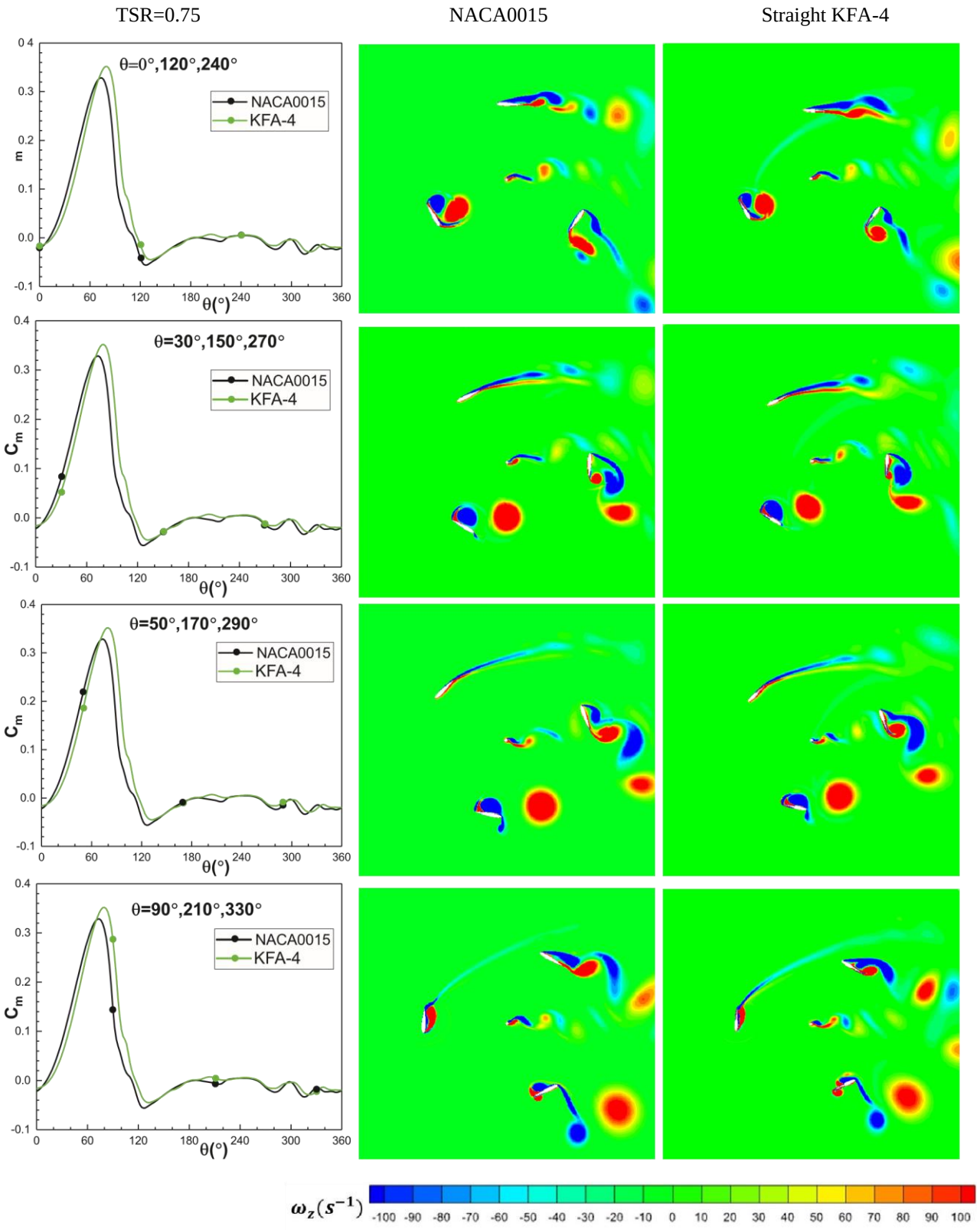

Fig. 28 torque coefficient and z-vorticity around baseline profile and straight KFA-4 design for different azimuthal positions at TSR=0.75

choose the optimum position of the step, its geometric shape, and the type of the KFA modification.

More information on the flow around the turbine can be gathered on the z-vorticity iso contours shown for the basic NACA0015 profile and the straight KFA-4 modified profile (Fig.18). As shown in Fig.27, Fig.28, Fig.29, and Fig.30, the contours are analyzed at different azimuthal positions of a reference blade (θ=0°,30°,50°,90°) for TSR=0.25, 0.75, 1.6 and 2.2, respectively. It is easy to see that the straight KFA-4 modification causes the delay in

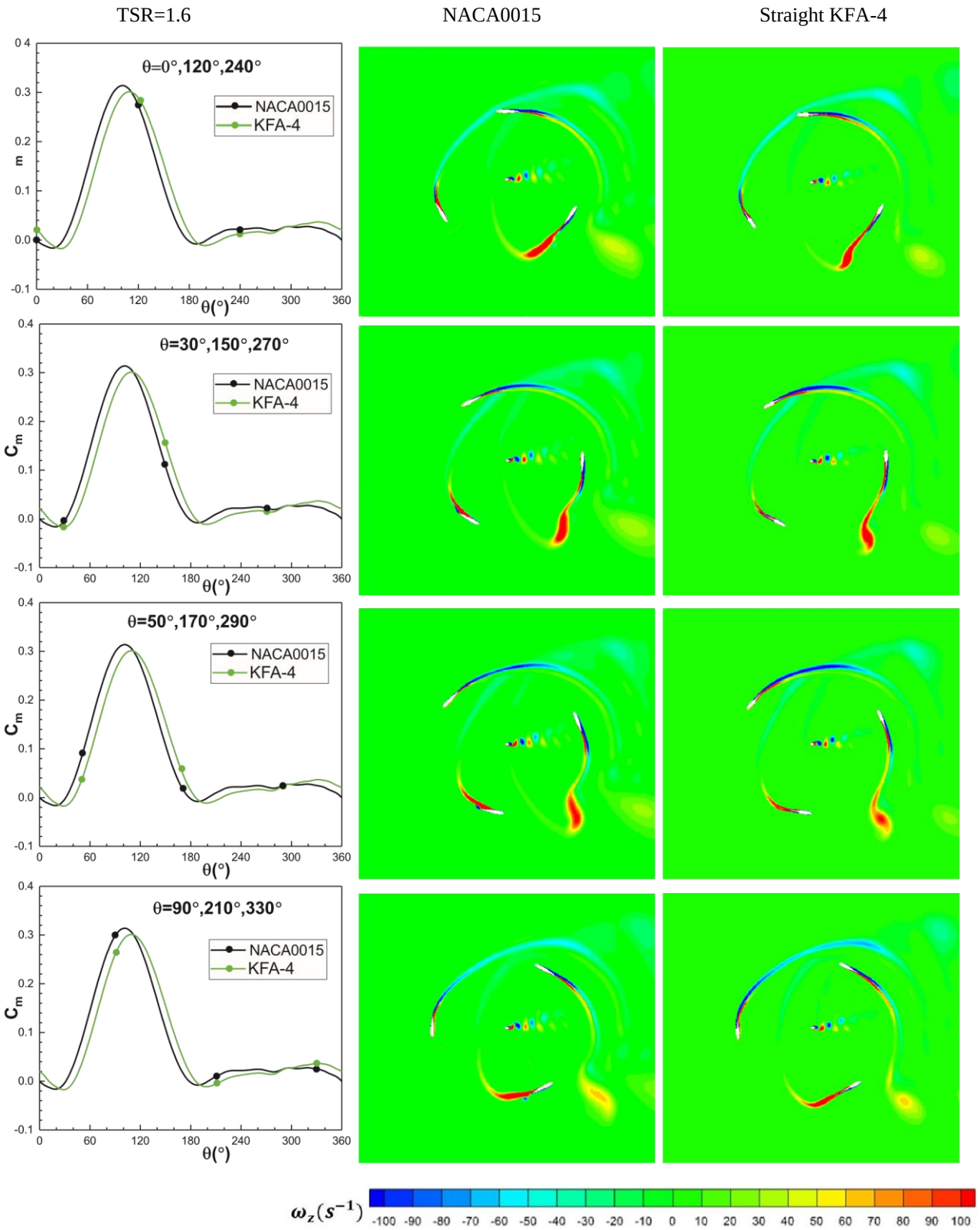

Fig. 29 torque coefficient and z-vorticity around baseline profile and straight KFA-4 design for different azimuthal positions at TSR=1.6

torque stall position that increases as a function of TSR. In the upstream phase, the straight KFA-4 produces vortices over the backward-facing step, accelerating the motion of the vortex structures close to the blade and delaying the torque stall. For TSR<1.6, the vortices detached from the blade are less dominant in the upstream phase, and their size is smaller in the downstream phase than in a conventional NACA0015 design. This means that in the unsteady case, the straight KFA-4 positively reduces the induced drag due to the recirculation zones. For TSR>1.6,

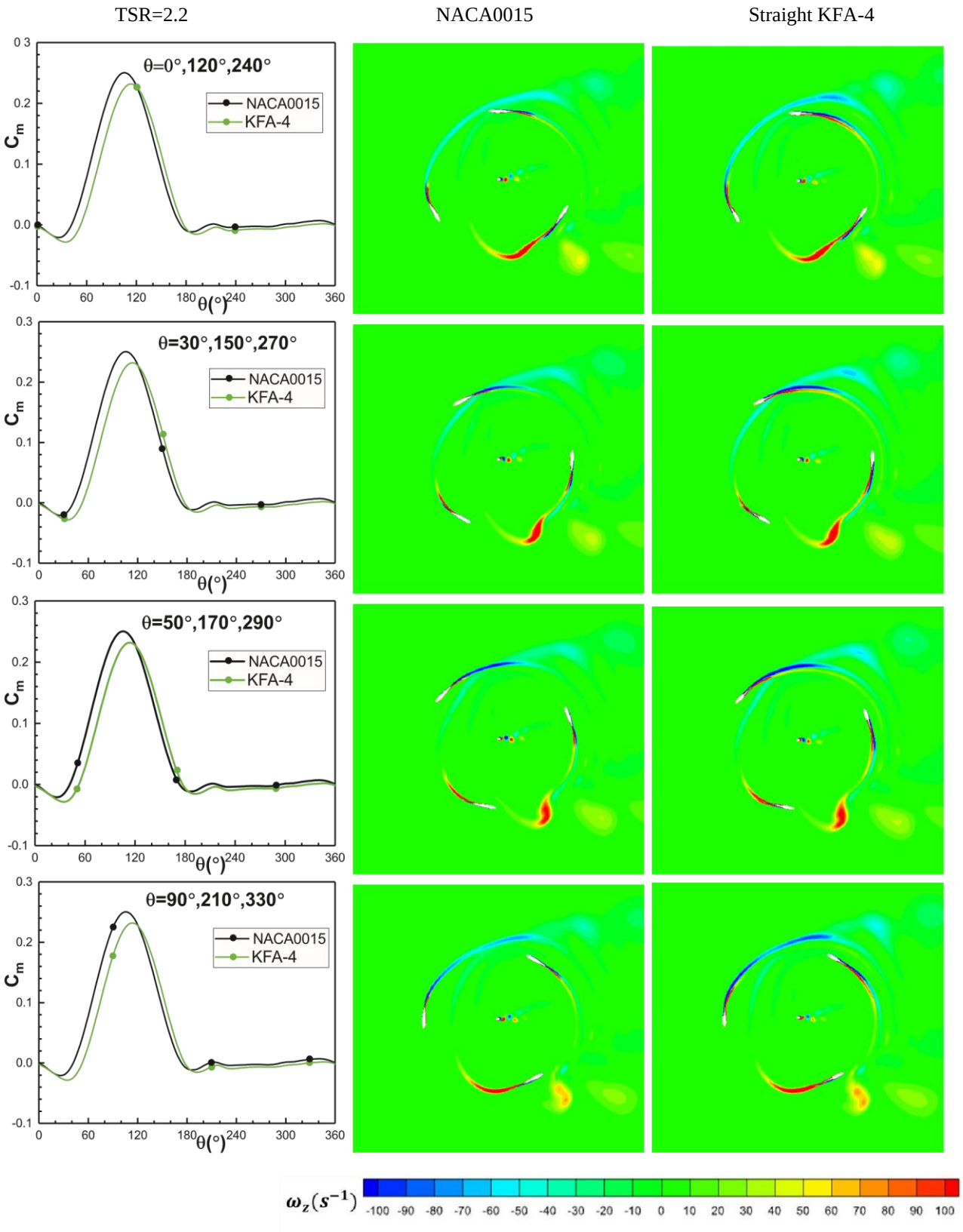

Fig. 30 torque coefficient and z-vorticity around baseline profile and straight KFA-4 design for different azimuthal positions at TSR=2.2

in the case of the modified blade design of the turbine, the dynamic stall and the blade/vortex interaction are more significant in the upstream phase, resulting in a loss of torque generation and, therefore, low power generation in this operating zone of the TSR compared to the basic NACA0015 design. At TSR= 1.6, the flow structure is quasi-similar sins the averaged C_m is almost identical for both designs resulting in similar power coefficient (power generation) as well.

4. CONCLUSION

A passive flow control method to enhance the efficiency of straight Darrieus wind turbines using Kline and Foglman Airfoil design is proposed in this work. A mid-chord step with a depth of 25% of the local relative thickness was introduced on the baseline profile NACA0015 according to the KFA-2 and KFA-4 designs.

In the first stage, a steady numerical study was carried out to investigate the effects of the top wall opening inclination and the shape of the leading edge of the backward-facing step on the aerodynamic efficiency of the profile for a large range of angles of attack ($-20^\circ \leq \alpha \leq 20^\circ$).

In the second stage, it was essential to design and evaluate the effectiveness of the optimal Kline and Fogleman design using a full VAWT configuration considering the effects of blade rotation and blade-wake interactions. A 2D unsteady numerical simulation was carried out using the finite volume method, of the flow around a three-bladed SD-VAWT designed by the symmetrical profile NACA0015 with a solidity of 0.48 and a turbine ratio of 1.2 for a TSR range of $0.25 \leq TSR \leq 2.4$. The main results of the investigation are summarized below:

(1) The 2D SST k-ω model overestimates the aerodynamic coefficients and power curve of static and dynamic blades, respectively. Moreover, the quadratic map mesh has a good capability of predicting the power curve with a reduced computational time compared to the triangular and quadratic pave meshes.

(2) Acute and right opening step angles are favorable for drag reduction, and obtuse angles are favorable for lift enhancement. KFA-4 is more efficient than the KFA-2 over the full range of positive and negative angles of attack. Moreover, the rounded step is better than the straight step for the KFA-4, and increasing the step curvature diameter causes a reduction in aerodynamic efficiency.

(3) The symmetrical straight KFA-4 blade design is better than the asymmetrical (straight KFA-2) for operating SD-VAWT.

(4) The effectiveness of the KFA blade design in improving the power generation of Lift-VAWTs varies with the TSR regime.

(5) The straight KFA-4 design has a positive effect on the starting torque, the delay of torque stall and vortex detachment, the reduction of the dead zone and the TSR corresponding to the nominal power, and the power curve for low TSRs ($TSR < 1.6$), the straight KFA-4 has a detrimental effect on the performance of the straight Darrieus wind turbine for high TSR ($TSR > 1.6$), due to the dominance of the blade/wake interaction on the upstream phase compared to the baseline NACA0015.

CONFLICT OF INTERESTS

The authors have no conflicts to disclose.

DATA AVAILABILITY

The data that support the findings of the study are available from corresponding author upon reasonable request.

AUTHORS CONTRIBUTIONS

Hemiche Iddou: Writing – original draft, Visualization, Validation, Software, Resources, Methodology, Investigation, Funding acquisition, Formal analysis, Data curation, Conceptualization; **Noura Nait Bouda:** Writing – review & editing, Supervision, Resources, Project administration, Methodology, Investigation, Funding acquisition, Conceptualization; **Azemi Benaissa:** Writing – review & editing, Supervision, Resources, Project administration, Investigation, Funding acquisition, Conceptualization; **Kacem Zereg:** Writing – review & editing, Writing – original draft, Visualization, Resources, Formal analysis.

REFERENCES

Akhlaghi, M., Asadbeigi, M., & Ghafoorian, F. (2023). Novel CFD and DMST dual method parametric study and optimization of a darrieus vertical axis wind turbine. *Journal of Applied Fluid Mechanics*, *17*(1), 205-218. https://www.jafmonline.net/article_2337.html

Amet, E., Maître, T., Pellone, C., & Achard, J. L. (2009). 2D numerical simulations of blade-vortex interaction in a darrieus turbine. *Journal of Fluids Engineering*, *131*(11), 111103. https://doi.org/10.1115/1.4000258

ANSYS Fluent user guide (2011). Ansys fluent theory guide. *Ansys Inc., USA*, *15317*, 724-746.

Apsley, D. D., & Leschziner, M. A. (2000). Advanced turbulence modelling of separated flow in a diffuser. *Flow, turbulence and combustion*, *63*, 81-112. https://doi.org/https://doi.org/10.1023/A:1009930107544

Arun Prakash, J., Radhakrishnan, S. S., Ramavijay, N., & Vishnupriya, S. (2017). Experimental investigation of stepped aerofoil using propeller test rig. *IJRET: International Journal of Research in Engineering and Technology*. https://doi.org/10.15623/ijret.2014.0308033

Aziz, M. A. B., & Islam, M. S. (2017). *Effect of lower surface modification on aerodynamic characteristics of an airfoil*. International Conference on Mechanical Engineering and Renewable Energy. https://www.cuet.ac.bd/icmere/files2017f/ICMERE2017-PI-250.pdf

Baxevanou, C. A., & Fidaros, D. K. (2008). Validation of numerical schemes and turbulence models combinations for transient flow around airfoil. *Engineering Applications of Computational Fluid Mechanics*, *2*(2), 208-221. https://doi.org/10.1080/19942060.2008.11015222

Boroomand, M., & Hosseinverdi, S. (2009). Numerical investigation of turbulent flow around a stepped

airfoil at high Reynolds number. *Fluids Engineering Division Summer Meeting*. https://doi.org/10.1115/FEDSM2009-78294

Bose Sumantraa, R., Chandramouli, S., Premsai T., P., Prithviraj, P., Mugundhan, V., & Velamati, R. K. (2014). Numerical analysis of effect of pitch angle on a small scale vertical axis wind turbine. *International Journal Of Renewable Energy Research*, *4*(4), 929–935. https://doi.org/10.20508/ijrer.v4i4.1653.g6463

Boudis, A., Benzaoui, A., Oualli, H., Guerri, O., Bayeul-Lain, A. C., & Coutier-Delgosha, O. (2018). Energy extraction performance improvement of a flapping foil by the use of combined foil. *Journal of Applied Fluid Mechanics*, 1651-1663. https://doi.org/10.29252/jafm.11.06.29099

Bravo, R., Tullis, S., & Ziada, S. (2007). *Performance testing of a small vertical-axis wind turbine*. Proceedings of the 21st Canadian Congress of Applied Mechanics. https://www.academia.edu/download/54779218/Performance_Testing_of_a_Small_Vertical-Axis_Wind_Turbine.pdf

Cardoso Netto, D., Ramirez Gustavo, R., & Manzanares Filho, N. (2023). Surrogate-based design optimization of a h-darrieus wind turbine comparing classical response surface, artificial neural networks, and kriging. *Journal of Applied Fluid Mechanics*, *16*(4), 703-716. https://doi.org/10.47176/jafm.16.04.1530

Danao, L. A., Qin, N., & Howell, R. (2012). A numerical study of blade thickness and camber effects on vertical axis wind turbines. *Proceedings of the Institution of Mechanical Engineers, Part A: Journal of Power and Energy*, *226*(7), 867-881. https://doi.org/10.1177/0957650912454403

Fertis. D. G., & Smith, L. L. (1986). Airfoil. United States Patent Number: US4606519A. https://patents.google.com/patent/US4606519A/en

Frunzulica, F., Dumitrache, A., & Suatean, B. (2014). *Numerical investigations of passive flow control elements for vertical axis wind turbine*. AIP Conference Proceedings. American Institute of Physics. https://www.fluid.tuwien.ac.at/322057?action=AttachFile&do=get&target=flu_ug.pdf

Gross, C. (2019). *Characterization of single-step Kline-Fogleman airfoils*. (Doctoral dissertation, Wichita State University). http://hdl.handle.net/10057/17146

Ismail, M. F., & Vijayaraghavan, K. (2015). The effects of aerofoil profile modification on a vertical axis wind turbine performance. *Energy*, *80*, 20-31. https://www.sciencedirect.com/science/article/pii/S0360544214012894

Jang, C. S., Ross, J. C., & Cummings, R. M. (1998). Numerical investigation of an airfoil with a Gurney flap. *Aircraft Design*, *1*(2), 75-88. https://www.sciencedirect.com/science/article/pii/S1369869980001 0X

Kabir, A., Islam, M., Jahan, N., Akib, Y. M., & Mili, M. I. J. (2021). Numerical simulation and comparative study of aerodynamic performance of Kline Fogleman modified backward stepped airfoils and the NACA 4415 airfoil. *Bangladesh Maritime Journal (BMJ) Volume*, *5*, 2520-1840. https://bsmrmu.edu.bd/public/files/econtents/6056f1d5c355f6-Numerical%20Simulation%20and%20Comparative%20Study%20of.pdf

Kozak, P. A., Vallverd, D., & Rempfer, D. (2016). Modeling vertical-axis wind-turbine performance: blade-element method versus finite volume approach. *Journal of Propulsion and Power*, *32*(3), 592-601. http://dx.doi.org/10.2514/1.B35550

Lanzafame, R., Mauro, S., & Messina, M. (2014). 2D CFD modeling of H-Darrieus wind turbines using a transition turbulence model. *Energy Procedia*, *45*, 131-140. https://doi.org/10.1016/j.egypro.2014.01.015

Lanzafame, R., Mauro, S., Messina, M., & Brusca, S. (2020). Development and validation of CFD 2D models for the simulation of micro H-Darrieus turbines subjected to high boundary layer instabilities. *Energies*, *13*(21), 5564. https://doi.org/10.3390/en13215564

Li, Y., Yang, S., Feng, F., & Tagawa, K. (2023). A review on numerical simulation based on CFD technology of aerodynamic characteristics of straight-bladed vertical axis wind turbines. *Energy Reports*, *9*, 4360-4379. https://doi.org/10.1016/j.egyr.2023.03.082

Lopez Mejia, O. D., Mejia, O. E., Escorcia, K. M., Suarez, F., & Laín, S. (2021). Comparison of sliding and overset mesh techniques in the simulation of a vertical axis turbine for hydrokinetic applications. *Processes*, *9*(11). https://www.mdpi.com/2227-9717/9/11/1933

Ma, N., Lei, H., Han, Z., Zhou, D., Bao, Y., Zhang, K., Zhou, L., & Chen, C. (2018). Airfoil optimization to improve power performance of a high-solidity vertical axis wind turbine at a moderate tip speed ratio. *Energy*, *150*, 236-252. https://www.sciencedirect.com/science/article/pii/S0360544218303499

Manerikar, S. S., Damkale, S. R., Havaldar, S. N., Kulkarni, S. V., & Keskar, Y. A. (2021). *Horizontal axis wind turbines passive flow control methods: a review*. IOP Conference Series: Materials Science and Engineering, I. O. P. Publishing. https://doi.org/10.1088/1757-899X/1136/1/012022

McLaren, K., Tullis, S., & Ziada, S. (2012). Computational fluid dynamics simulation of the aerodynamics of a high solidity, small-scale vertical axis wind turbine. *Wind Energy*, *15*(3), 349-361. https://doi.org/10.1002/we.472

Meana-Fernández, A., Solís-Gallego, I., Fernández Oro, J. M., Argüelles Díaz, K. M., & Velarde-Suárez, S. (2018). Parametrical evaluation of the aerodynamic performance of vertical axis wind turbines for the

proposal of optimized designs. *Energy*, *147*, 504-517. https://doi.org/https://doi.org/10.1016/j.energy.2018.01.062

Menter, F. R. (1994). Two-equation eddy-viscosity turbulence models for engineering applications. *AIAA Journal*, *32*(8), 1598-1605. https://doi.org/10.2514/3.12149

Modi, F. N., & Gilke, N. R. (2018). *Computational analysis of various airfoil profile on the performance of h-Darrieus wind turbine.* 2018 Ieee International Conference On System, Computation, Automation And Networking (Icscan), IEEE. https://doi.org/10.1109/ICSCAN.2018.8541245

Moghimi, M., & Motawej, H. J. J. O. A. F. M. (2020). Comparison aerodynamic performance and power fluctuation between darrieus straight-bladed and gorlov vertical axis wind turbines. *Journal of Applied Fluid Mechanics*, *13*(5), 1623-1633. https://doi.org/10.36884/jafm.13.05.30833

Mohamed, M. H. (2012). Performance investigation of H-rotor Darrieus turbine with new airfoil shapes. *Energy*, *47*(1), 522-530. https://www.sciencedirect.com/science/article/pii/S0360544212006755

Mohammed, A. A., Ouakad, H. M., Sahin, A. Z., & Bahaidarah, H. M. S. (2019). Vertical axis wind turbine aerodynamics: summary and review of momentum models. *Journal of Energy Resources Technology*, *141*(5), 050801. https://doi.org/10.1115/1.4042643

Mohan Kumar, P., Sivalingam, K., Lim, T.-C., Ramakrishna, S., & Wei, H. (2019). review on the evolution of darrieus vertical axis wind turbine: large wind turbines. *Clean Technologies*, *1*(1), 205-223. https://www.mdpi.com/2571-8797/1/1/14

Olsman, W. F. J., & Colonius, T. (2011). Numerical simulation of flow over an airfoil with a cavity. *AIAA journal*, *49*(1), 143-149. https://doi.org/10.2514/1.J050542

Qadri, M., Shahzad, A., Zhao, F., & Tang, H. (2019). An experimental investigation of a passively flapping foil in energy harvesting mode. *Journal of Applied Fluid Mechanics*, *12*(5), 1547-1561. https://doi.org/10.29252/jafm.12.05.29648

Qamar, S. B., & Janajreh, I. (2017). A comprehensive analysis of solidity for cambered darrieus VAWTs. *International Journal of Hydrogen Energy*, *42*(30), 19420-19431. https://doi.org/https://doi.org/10.1016/j.ijhydene.2017.06.041

Rezaeiha, A., Montazeri, H., & Blocken, B. (2019). On the accuracy of turbulence models for CFD simulations of vertical axis wind turbines. *Energy*, *180*, 838-857. https://doi.org/https://doi.org/10.1016/j.energy.2019.05.053

Rogowski, K., Hansen, M. O. L., & Bangga, G. (2020). Performance analysis of a H-darrieus wind turbine for a series of 4-digit NACA airfoils. *Energies*, *13*(12). https://www.mdpi.com/1996-1073/13/12/3196

Roh, S. C., & Kang, S. H. (2013). Effects of a blade profile, the Reynolds number, and the solidity on the performance of a straight bladed vertical axis wind turbine. *Journal of Mechanical Science and Technology*, *27*(11), 3299-3307. https://doi.org/10.1007/s12206-013-0852-x

Rumsey, C. (2017). *NASA langley research center turbulence modeling resource*. NASA Langley Research Center, Hampton, VA, https://turbmodels.larc.nasa.gov/

Sagharichi, A., Maghrebi, M. J., & ArabGolarcheh, A. (2016). Variable pitch blades: An approach for improving performance of Darrieus wind turbine. *Journal of Renewable and Sustainable Energy*, *8*(5), 053305. https://doi.org/10.1063/1.4964310

Sammak, S., Mojgani, R., & Boroomand, M. (2012). *Transitional CFD Investigation of Stepped Airfoil.* THMT-12. Proceedings of the Seventh International Symposium On Turbulence Heat and Mass Transfer, Begel House. https://doi.org/10.1615/ICHMT.2012.ProcSevIntSympTurbHeatTransfPal.2190

Sheldahl, R. E., & Klimas, P. C. (1981). *Aerodynamic characteristics of seven symmetrical airfoil sections through 180-degree angle of attack for use in aerodynamic analysis of vertical axis wind turbines* (No. SAND-80-2114). Sandia National Lab.(SNL-NM), Albuquerque, NM (United States). https://www.osti.gov/biblio/6548367

Sobhani, E., Ghaffari, M., & Maghrebi, M. J. (2017). Numerical investigation of dimple effects on darrieus vertical axis wind turbine. *Energy*, *133*, 231-241. https://www.sciencedirect.com/science/article/pii/S0360544217308617

Song, C., Wu, G., Zhu, W., & Zhang, X. (2020). Study on aerodynamic characteristics of Darrieus vertical axis wind turbines with different airfoil maximum thicknesses through computational fluid dynamics. *Arabian Journal for Science and Engineering*, *45*, 689-698. https://doi.org/10.1007/s13369-019-04127-8

Storms, B. L., & Jang, C. S. (1994). Lift enhancement of an airfoil using a Gurney flap and vortex generators. *Journal of Aircraft*, *31*(3), 542-547. https://doi.org/10.2514/3.46528

Subramanian, A., Yogesh, S. A., Sivanandan, H., Giri, A., Vasudevan, M., Mugundhan, V., & Velamati, R. K. (2017). Effect of airfoil and solidity on performance of small scale vertical axis wind turbine using three dimensional CFD model. *Energy*, *133*, 179-190. https://www.sciencedirect.com/science/article/pii/S0360544217308757

Sun, X., Xu, Y., & Huang, D. (2019). Numerical simulation and research on improving aerodynamic performance of vertical axis wind turbine by co-flow

jet. *Journal of Renewable and Sustainable Energy*, *11*(1). https://doi.org/10.1063/1.5052378

Syawitri, T. P., Yao, Y., Yao, J., & Chandra, B. (2022). A review on the use of passive flow control devices as performance enhancement of lift-type vertical axis wind turbines. *Wiley Interdisciplinary Reviews: Energy and Environment*, *11*(4), e435. https://doi.org/10.1002/wene.435

Truong, H. V. A., Dang, T. D., Vo, C. P., & Ahn, K. K. (2022). Active control strategies for system enhancement and load mitigation of floating offshore wind turbines: A review. *Renewable and Sustainable Energy Reviews*, *170*, 112958. https://doi.org/10.1016/j.rser.2022.112958

Wang, H., Zhang, B., Qiu, Q., & Xu, X. (2017). Flow control on the NREL S809 wind turbine airfoil using vortex generators. *Energy*, *118*, 1210-1221. https://www.sciencedirect.com/science/article/pii/S0360544216315924

Wang, X., Luo, X., Zhuang, B., Yu, W., & Xu, H. (2011). *6-DOF numerical simulation of the vertical-axis water turbine*. Fluids Engineering Division Summer Meeting. https://doi.org/10.1115/AJK2011-22035

Wang, Y., Shen, S., Li, G., Huang, D., & Zheng, Z. (2018). Investigation on aerodynamic performance of vertical axis wind turbine with different series airfoil shapes. *Renewable Energy*, *126*, 801-818. https://www.sciencedirect.com/science/article/pii/S0960148118302398

Wekesa, D. W., Wang, C., Wei, Y., Kamau, J. N., & Danao, L. A. M. (2015). A numerical analysis of unsteady inflow wind for site specific vertical axis wind turbine: A case study for Marsabit and Garissa in Kenya. *Renewable Energy*, *76*, 648-661. https://www.sciencedirect.com/science/article/pii/S0960148114008052

Winslow, J., Otsuka, H., Govindarajan, B., & Chopra, I. (2018). Basic understanding of airfoil characteristics at low reynolds numbers (104–105). *Journal of Aircraft*, *55*(3), 1050-1061. https://doi.org/10.2514/1.C034415

Xie, Y. H., Jiang, W., Lu, K., & Zhang, D. (2016). Numerical investigation into energy extraction of flapping airfoil with Gurney flaps. *Energy*, *109*, 694-702. https://www.sciencedirect.com/science/article/pii/S0360544216306491

Zamani, M., Maghrebi, M. J., & Varedi, S. R. (2016a). Starting torque improvement using J-shaped straight-bladed Darrieus vertical axis wind turbine by means of numerical simulation. *Renewable Energy*, *95*, 109-126. https://www.sciencedirect.com/science/article/pii/S0960148116302531

Zamani, M., Nazari, S., Moshizi, S. A., & Maghrebi, M. J. (2016b). Three dimensional simulation of J-shaped Darrieus vertical axis wind turbine. *Energy*, *116*, 1243-1255. https://www.sciencedirect.com/science/article/pii/S0360544216314529

Zhang, L., Shan, X., & Xie, T. (2020). Active control for wall drag reduction: Methods, mechanisms and performance. *IEEE Access*, *8*, 7039-7057. https://doi.org/10.1109/ACCESS.2020.2963843

Zhao, Z., Wang, D., Wang, T., Shen, W., Liu, H., & Chen, M. (2022). A review: Approaches for aerodynamic performance improvement of lift-type vertical axis wind turbine. *Sustainable Energy Technologies and Assessments*, *49*, 101789. https://www.sciencedirect.com/science/article/pii/S2213138821008031

Zhao, Z., Wang, R., Shen, W., Wang, T., Xu, B., Zheng, Y., & Qian, S. (2018). Variable pitch approach for performance improving of straight-bladed VAWT at rated tip speed ratio. *Applied Sciences*, *8*(6). https://www.mdpi.com/2076-3417/8/6/957